

Evolution of Holocene dacite and compositionnally zoned magma, volcan San Pedro, Southern volcanic zone, Chile.

Fidel Costa Rodriguez, Brad Singer

▶ **To cite this version:**

Fidel Costa Rodriguez, Brad Singer. Evolution of Holocene dacite and compositionnally zoned magma, volcan San Pedro, Southern volcanic zone, Chile.. Journal of Petrology, 2002, 43 (8), pp.1571-1593. 10.1093/petrology/43.8.1571 . hal-00077612

HAL Id: hal-00077612
https://insu.hal.science/hal-00077612

Submitted on 8 Mar 2019

HAL is a multi-disciplinary open access archive for the deposit and dissemination of scientific research documents, whether they are published or not. The documents may come from teaching and research institutions in France or abroad, or from public or private research centers.

L'archive ouverte pluridisciplinaire **HAL**, est destinée au dépôt et à la diffusion de documents scientifiques de niveau recherche, publiés ou non, émanant des établissements d'enseignement et de recherche français ou étrangers, des laboratoires publics ou privés.

JOURNAL OF PETROLOGY | VOLUME 43 | NUMBER 8 | PAGES 1571–1593 | 2002

Evolution of Holocene Dacite and Compositionally Zoned Magma, Volcán San Pedro, Southern Volcanic Zone, Chile

FIDEL COSTA[1] AND BRAD SINGER[2]*

[1]INSTITUT DES SCIENCES DE LA TERRE D'ORLÉANS-CNRS, 1A RUE DE LA FÉROLLERIE, ORLÉANS 45071, FRANCE
[2]DEPARTMENT OF GEOLOGY AND GEOPHYSICS, UNIVERSITY OF WISCONSIN–MADISON, 1215 WEST DAYTON STREET, MADISON WI 53076, USA

RECEIVED AUGUST 6, 2001; REVISED TYPESCRIPT ACCEPTED FEBRUARY 21, 2002

Volcán San Pedro in the Andean Southern Volcanic Zone (SVZ) Chile, comprises Holocene basaltic to dacitic lavas with trace element and strontium isotope ratios more variable than those of most Pleistocene lavas of the underlying Tatara–San Pedro complex. Older Holocene activity built a composite cone of basaltic andesitic and silicic andesitic lavas with trace element ratios distinct from those of younger lavas. Collapse of the ancestral volcano triggered the Younger Holocene eruptive phase including a sequence of lava flows zoned from high-K calc-alkaline hornblende–biotite dacite to two-pyroxene andesite. Notably, hornblende–phlogopite gabbroic xenoliths in the dacitic lava have relatively low $^{87}Sr/^{86}Sr$ ratios identical to their host, whereas abundant quenched basaltic inclusions are more radiogenic than any silicic lava. The latest volcanism rebuilt the modern 3621 m high summit cone from basaltic andesite that is also more radiogenic than the dacitic lavas. We propose the following model for the zoned magma: (1) generation of hornblende–biotite dacite by dehydration partial melting of phlogopite-bearing rock similar to the gabbroic xenoliths; (2) forceful intrusion of basaltic magma into the dacite, producing quenched basaltic inclusions and dispersion of olivine and plagioclase xenocrysts throughout the dacite; (3) cooling and crystallization–differentiation of the basalt to basaltic andesite; (4) mixing of the basaltic andesite with dacite to form a small volume of two-pyroxene hybrid andesite. The modern volcano comprises basaltic andesite that developed independently from the zoned magma reservoir. Evolution of dacitic and andesitic magma during the Holocene and over the past 350 kyr reflects the intrusion of multiple mafic magmas that on occasion partially melted or assimilated hydrous gabbro within the shallow crust. The chemical and isotopic zoning of Holocene magma at Volcán San Pedro is paralleled by that of historically erupted magma at neighboring Volcán Quizapu. Consequently, the role of young, unradiogenic hydrous gabbro in generating dacite and contaminating basalt may be underappreciated in the SVZ.

KEY WORDS: *Andes; dacite; gabbro; Holocene; strontium isotopes*

INTRODUCTION

The origin of compositional zoning in magma erupted within volcanic arcs remains controversial (Eichelberger *et al.*, 2000, 2001; de Silva, 2001). It has been investigated at several localities and scales including relatively large systems such as the >550 km^3 Calabozos complex (Grunder & Mahood, 1988) and 50 km^3 Crater Lake (Bacon & Druitt, 1988; Druitt & Bacon, 1989), intermediate-sized systems such as the 15 km^3 Valley of Ten Thousand Smokes (Hildreth, 1987), 9 km^3 Quizapu (Hildreth & Drake, 1992) and 4 km^3 Giant Crater–Medicine Lake (Baker *et al.*, 1991), and much smaller 0·1–1·4 km^3 eruptions such as Paricutin, Arenal, and Rishiri (Wilcox, 1954; McBirney *et al.*, 1987; Reagan *et al.*, 1987; Kuritani, 2001). Whereas explosive eruptions like those at Quizapu, Crater Lake, and Valley of Ten Thousand Smokes can provide an instantaneous sampling of a zoned magma, particularly revealing records occur as well in historical or Holocene lavas and tephras at Medicine Lake, Paricutin, Arenal, and Rishiri, where superposition of different flows permits reconstruction of the magma reservoir.

*Corresponding author. Telephone: 001-608-265-8650. Fax: 001-608-262-0693. E-mail: bsinger@geology.wisc.edu

© Oxford University Press 2002

Moreover, shifts in erupted magma composition over short periods of time may illuminate time scales for both differentiation processes and the invasion of subvolcanic plumbing systems by new batches of magma (Singer *et al.*, 1995; Hobden *et al.*, 1999).

This paper focuses on a sequence of lava flows of 1 km^3 that erupted during the Holocene from a strongly zoned body of magma beneath the composite Volcán San Pedro in the Southern Volcanic Zone of the Chilean Andes. The lava ranges from biotite–hornblende dacite (66 wt % SiO_2) to a two-pyroxene dacite (64 wt % SiO_2) that contains quenched inclusions of basalt (52 wt % SiO_2), andesite (61 wt % SiO_2), and basaltic andesite (55–57 wt % SiO_2). Whereas petrographic and mineralogical evidence for physical mingling of basaltic and dacitic magmas is clear (Singer *et al.*, 1995), the importance of hybridization via magma mixing, crustal assimilation, liquid fractionation, and crystallization remain poorly known. On the basis of a combination of geological mapping, petrography, whole-rock chemical compositions, and Sr isotope data we provide insight into the physical processes that contributed to the pre-eruptive chemical zoning. Further, the petrographic and geochemical character of the zoned late Holocene magma is compared with the preceding eruptions of dacite and andesite during the latest Pleistocene and earlier Holocene to highlight the number and diversity of magma batches and magmatic processes that have occurred over the past ~350 kyr.

Volcán San Pedro grew at the arc front on crust that is probably 35–40 km thick along the transect from which Hildreth & Moorbath (1988) obtained geochemical and isotopic data that led to the hypothesis of lower-crustal Melting, Assimilation, Storage and Homogenization (MASH) for continental arc magmatism. Geochemical and isotopic surveys by Davidson *et al.* (1987, 1988) further indicated that crustal contamination and mixing were important processes at Volcán San Pedro and the underlying volcanic complex. By addressing in detail the origin of the dacitic magma, how it came to be juxtaposed with basalt before eruption, and the nature of the mafic magma that subsequently recharged the plumbing system, we explore subvolcanic processes taking place above the proposed deep crustal MASH zone of Hildreth & Moorbath (1988).

GEOLOGY OF VOLCÁN SAN PEDRO

Volcán San Pedro is the composite ~2 km^3 edifice capping the Quaternary Tatara–San Pedro complex (TSPC) at 36°S, 71°50′W in the Southern Volcanic Zone (SVZ) of the Chilean Andes (Fig. 1). Except for small neoglacial moraines, San Pedro is unglaciated, and therefore is of Holocene age. Throughout this paper we will distinguish

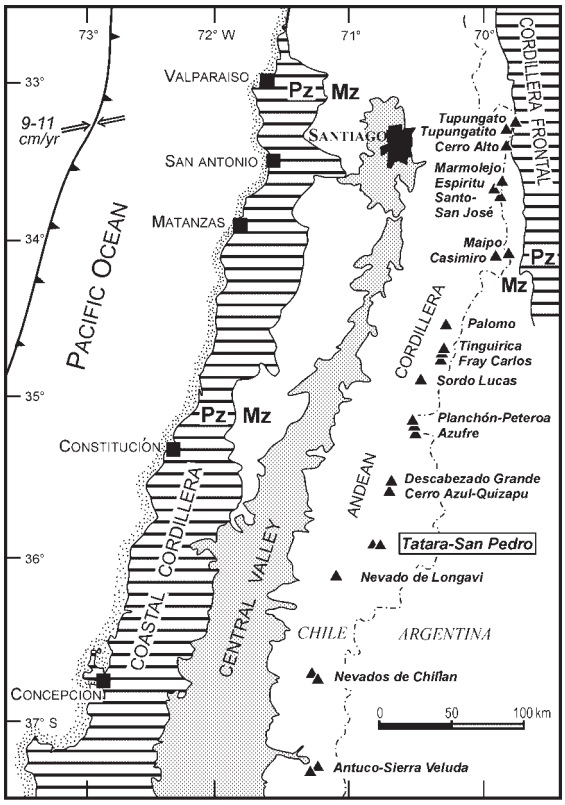


Fig. 1. Geological setting and location of Volcán San Pedro in the Southern Volcanic Zone of the Chilean Andes. Paleozoic (PZ) rocks crop out in the Coastal Cordillera and Cordillera Frontal, whereas Mesozoic (MZ) rocks crop out beneath the axis of the Andean Cordillera, which is also locally intruded or overlain by Cenozoic rocks not shown for clarity. The Central Valley comprises Neogene and Quaternary sediment overlying Mesozoic basement. Modified from Hildreth & Moorbath (1988), who inferred that the crust thins markedly southward from ~55–65 km between 33 and 34°S to ~35–40 km between 36 and 37°S.

between two periods of volcanic activity (Fig. 2a; Table 1): the Older Holocene during which a composite cone of ~1 km^3 grew, and the Younger Holocene during which an additional ~1 km^3 of lavas that post-date collapse of the southeastern flank of the ancestral cone were erupted, including the modern summit cone of Volcán San Pedro. The latter reflects the most recent volcanic activity that spanned the last 930 kyr at the TSPC (Singer *et al.*, 1997).

Older Holocene lavas are mainly basaltic andesites that erupted from a central vent at ~3500 m above sea level and flowed into valleys glacially incised through the Volcán Tatara shield (Fig. 2b). A silicic andesite (62 wt % SiO_2) from this unit was also described by Ferguson *et al.* (1992), however. We present new data from three basaltic andesitic lava flows and a silicic andesite flow sampled near its head at about 3500 m (Fig. 2a and b). Field relations do not reveal whether basaltic andesitic or the silicic andesitic lavas erupted first.

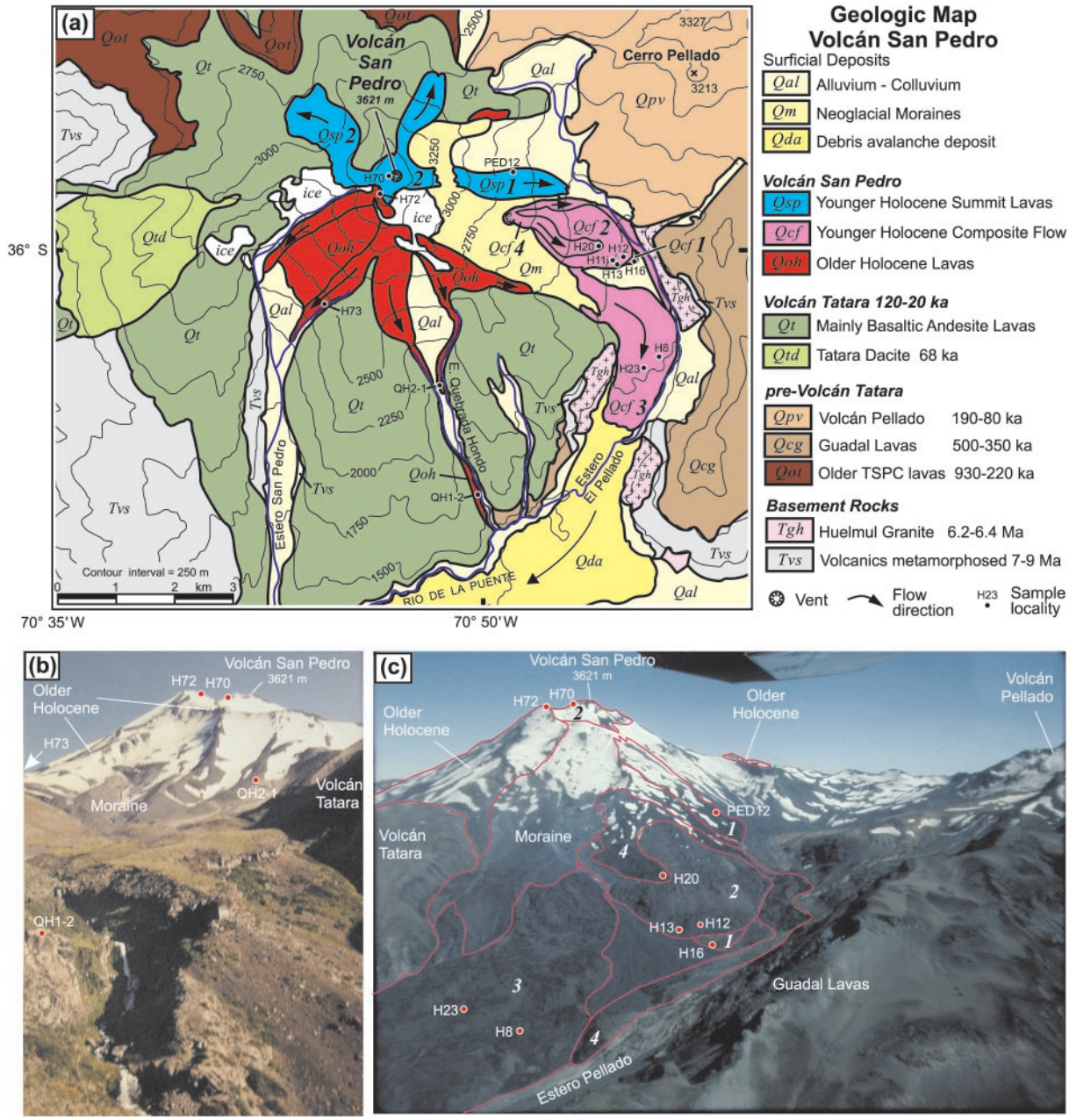


Fig. 2. (a) Geological map of Volcán San Pedro showing localities of samples. (b) View of San Pedro from the south at 1600 m above sea level in Estero Quebrada Hondo. (c) San Pedro from a light aircraft, view to the NW. Field relations of the Younger Holocene lavas are clearly visible.

Younger Holocene volcanism began after southeastward collapse of the 1500 m tall cone produced a 13 km long, ~4 km^3 debris avalanche deposit that flowed down Estero Pellado and Rio de la Puente valleys (Fig. 1a; Ferguson *et al.*, 1992; Singer *et al.*, 1995, 1997). The ensuing eruption of an airfall tephra and the strongly zoned composite San Pedro flow may have been triggered by this sector collapse. The small yet distinctive biotite–hornblende-phyric dacitic lava that forms the earliest emplaced head of the composite flow is designated Qcf 1 (Fig. 2a and c). The Qcf 1 flow was buried by a similar, more voluminous but less silicic lava, Qcf 2, that hosts rare quenched basaltic inclusions and 2–3 vol. % of angular gabbroic xenoliths 5–50 cm in diameter. These xenoliths, described in detail by Costa *et al.* (2002), comprise both coarse-grained Late Miocene hornblende-

Table 1: Eruptive sequence, composition, mineralogy, and main petrological features of the Older and Younger Holocene lava flows of Volcán San Pedro; Younger Holocene map units arranged from oldest at bottom to youngest at top

Map unit	Sample no.	SiO_2 (wt %)	Phenocryst minerals	Volume (km^3)	Description and comments
Younger Holocene					
San Pedro summit-forming eruptions					
Qsp 2	H-70	56·7	Pl, Ol, Cpx, Opx, Mt	0·1	Latest flows form modern San Pedro summit spatter cone
Qsp 1	PED-12	55·5	Pl, Ol, Cpx, Mt	0·1	Early flow from summit vent
Composite zoned San Pedro flow					
Qcf 4	H-20	61·4	Pl, Cpx, Opx, Mt, Ilm	0·1	Latest eruption from pre-summit vents, contains <1%
	H-20i	57·3	Pl, Ol, Cpx, Hbl, Mt		basaltic andesite inclusions, Ol + Pl xenocrysts
Qcf 3	H-23	63·7	Pl, Cpx, Opx, Mt, Ilm	0·5	Composite multi-lobate flow, contains 1–20% basaltic
	H-8	63·6	Pl, Cpx, Opx, Mt, Ilm		inclusions Ol + Pl xenocrysts; rare Hbl and Bt with reaction rims
	H-23i	52·4	Pl, Ol, Cpx, Opx, Hbl, Mt		
	H-8i	52·5	Pl, Ol, Cpx, Mt		
Qcf 2	H-12	64·5	Pl, Cpx, Opx, Hbl, Bt, Mt, Ilm	0·2	Dacite contains 0·1% quenched basaltic inclusions and
	H-13	64·6	Pl, Cpx, Opx, Hbl, Bt, Mt, Ilm		5% angular hornblende–phlogopite-bearing gabbroic
	H-11i	51·5	Pl, Ol, Cpx, Hbl, Mt		xenoliths
Qcf 1	H-16	65·8	Pl, Cpx, Opx, Hbl, Bt, Mt, Ilm	<0·01	Small lobe of dacite, lacks xenoliths, contains Ol + Pl xenocrysts
Older Holocene					
Qoh	H-73	55·4	Pl, Ol, Cpx, Opx, Mt	1·0	Basaltic andesite flows of Estero San Pedro and
	QH1-1	54·8	Pl, Ol, Cpx, Mt		Quebrada Hondo
	QH1-2	53·9	Pl, Ol, Cpx, Mt		
	H-72	62·2	Pl, Cpx, Opx, Mt	<0·05	Andesite flow of upper Estero San Pedro—near modern summit

Letter 'i' in sample number designates a quenched inclusion. Pl, plagioclase; Ol, olivine; Cpx, clinopyroxene; Opx, orthopyroxene; Hbl, hornblende; Bt, biotite; Mt, magnetite; Ilm, ilmenite.

and phlogopite-bearing gabbroic rocks and incompletely solidified, possibly comagmatic (Holocene) gabbro. A larger two-pyroxene dacitic lava, Qcf 3, containing 5–10 vol. % of quenched basaltic inclusions up to 20 cm across (Fig. 3) erupted next, accompanied by mingled airfall tephra of identical composition (Ferguson *et al.*, 1992; Singer *et al.*, 1995). The Qcf 3 flow was followed by a small two-pyroxene andesite lava, Qcf 4, that erupted from a vent that developed into a small scoria-spatter cone above the Qcf 2 dacite (Fig. 2a and c).

These eruptions took place following the last major retreat of ice after 23 ka (Singer *et al.*, 2000), which preceded the growth and collapse of the ancestral San Pedro cone (Qoh lavas, Fig. 2). The Qcf lavas are partly buried by and therefore older than small neoglacial moraines <1000 years old and the modern summit cone lavas (Fig. 2). No ash or soil deposits separate the morphologically pristine glassy Qcf flows from one another. Thus, whereas the eruptions from a common vent system that produced the composite zoned San Pedro flow may have persisted up to several thousand years, they just as likely lasted no more than a few centuries or decades.

A basaltic andesitic lava flow, designated Qsp 1, formed part of the eastern slope of Volcán San Pedro and erupted from a now eroded or buried vent high on the eastern flank of the edifice (Fig. 2a and c). We interpret the Qsp 1 lava to represent the initiation of volcanism that built the modern San Pedro summit cone. The youngest eruptions were of basaltic andesite ($\sim 0{\cdot}1\ km^3$), designated Qsp 2, that form the modern 3621 m high summit scoria cone and lava flows that are unglaciated (Fig. 2a and c). To help guide the petrological and geochemical discussion that follows, the eruptive history and character of the Older Holocene and Younger Holocene lavas are summarized in Table 1.

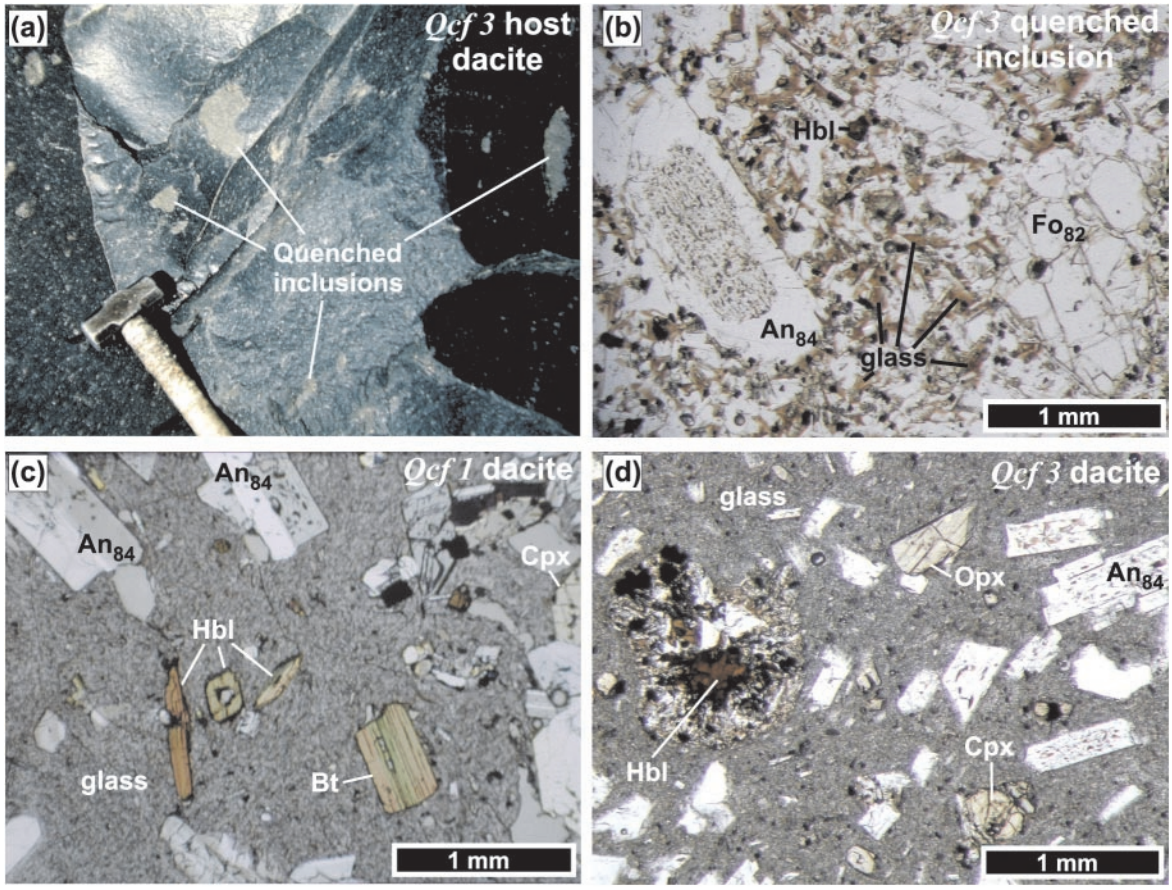


Fig. 3. Petrography of dacite and quenched basaltic inclusions in dacites forming the composite San Pedro lava flow. (a) Outcrop near locality H-23 in Fig. 2c. Grey inclusions up to 20 cm across have crenulated margins and form up to 20% of outcrops within the black glassy dacite host lava. (b) Photomicrograph of quenched basaltic inclusion H-23i; plane-polarized light. A few small hornblende crystals and large forsterite and anorthite crystals are surrounded by plagioclase microlites and interstitial brown glass. (c) Photomicrograph of sample H-16 from Qcf 1 dacite; plane-polarized light. Euhedral biotite, hornblende, augite, plagioclase, and magnetite are visible. Larger sieve-cored An_{84} plagioclase crystals are similar to those in (b) and probably are xenocrysts. (d) Photomicrograph of sample H-23 from Qcf 3 dacite illustrating the rare anhedral and strongly resorbed hornblende crystals with orthopyroxene + plagioclase + magnetite reaction rims; plane-polarized light. An, anorthite; Bt, biotite; Hbl, hornblende; Fo, forsterite; Cpx, clinopyroxene; Opx, orthopyroxene.

From these observations we infer that: (1) the composite San Pedro flow—including in eruptive order flow lobes Qcf 1, Qcf 2, Qcf 3 and Qcf 4—reflects rapid and nearly complete withdrawal of magma from successively deeper levels of a strongly zoned chamber that contained biotite–hornblende dacite at its roof, and less silicic two-pyroxene andesite in its lower reaches; (2) basaltic and dacitic magma coexisted and mechanically mingled within the zoned chamber; (3) before the collapse of ancestral San Pedro, the wall-rocks of this zoned magma reservoir comprised, in part, Miocene gabbroic plutonic rocks or incompletely solidified gabbro, blocks of which were incorporated into the magma during the collapse and entrained in rapidly ascending viscous dacitic magma; (4) the plumbing system was replenished with basaltic andesitic magma that subsequently erupted to build the modern composite cone to its present height (Fig. 2c).

The range of basaltic to dacitic compositions forming the Younger Holocene lavas contrast markedly with $\sim 10\ km^3$ of basaltic andesitic lavas (52–56 wt % SiO_2) that formed the younger part of the underlying Volcán Tatara shield during latest Pleistocene between about 70 and 20 ka (Davidson *et al.*, 1988; Ferguson *et al.*, 1992; Singer *et al.*, 1997; Dungan *et al.*, 2001). The lowermost portion of Volcán Tatara was erupted between 100 and 70 ka and is also dominantly composed of $\sim 10\ km^3$ of basaltic andesitic lavas that are capped by an $\sim 1\ km^3$ dacite flow that is distinguished from the Younger Holocene dacite by the absence of petrographic and mineralogical evidence of mingling or mixing with mafic magma (Fig. 2a; Singer *et al.*, 1995). Although the focus of this paper is on the Younger Holocene lavas, we place these into an expanded temporal context by providing salient geochemical background on the latest Pleistocene Guadal and Tatara dacites (Fig. 2a

Table 2: Major element, trace element, Sr isotope, and modal compositions of Holocene San Pedro lavas and quenched magmatic inclusions

	Younger Holocene lavas and inclusions									
	San Pedro composite flow						Composite flow-quenched inclusions			
Map unit:	Qcf 1	Qcf 2	Qcf 2	Qcf 3	Qcf 3	Qcf 4	Qcf 2	Qcf 3	Qcf 3	Qcf 4
Sample:	H-16	H-13	H-12	H-23	H-8	H-20	H-11i	H-8i	H-23i	H-20i
wt %										
SiO_2	65·8	64·6	64·5	63·7	63·6	61·4	51·5	52·5	52·4	57·3
TiO_2	0·51	0·58	0·60	0·64	0·65	0·74	1·02	0·99	0·99	1·16
Al_2O_3	16·26	16·44	16·53	16·75	16·78	16·99	18·19	17·35	17·24	17·85
FeO	3·74	4·18	4·29	4·52	4·53	5·24	8·29	8·60	8·48	7·21
MnO	0·08	0·09	0·09	0·09	0·09	0·10	0·15	0·15	0·15	0·15
MgO	1·78	2·16	2·33	2·29	2·35	2·89	5·89	7·37	7·42	3·13
CaO	4·08	4·51	4·59	4·80	4·82	5·54	10·06	8·01	8·07	6·75
Na_2O	4·54	4·35	4·31	4·35	4·31	4·27	3·31	3·23	3·27	4·23
K_2O	2·70	2·57	2·52	2·46	2·46	2·17	0·88	1·02	1·09	1·62
P_2O_5	0·16	0·17	0·18	0·19	0·20	0·21	0·17	0·24	0·22	0·32
Total	100·0	100·1	100·4	100·3	100·3	100·2	100·4	100·4	100·3	100·5
Fe_2O_3	4·16	4·64	4·77	5·02	5·03	5·82	9·21	9·56	9·42	8·01
ppm										
Rb	95	89	86	88	84	71	21	31	31	43
Cs	4·6	4·2		4·2		3·3	0·8		1·0	1·3
Sr	452	458	461	482	473	504	454	586	564	570
Ba	618	577	562	563	563	525	212	353	330	383
Sc	8·0	9·8		10·7		13·1	25·2		22·1	17·1
V	54	64		73	82	97	214	173	173	124
Cr	15	24	28	23	26	36	148	172	179	b.d.
Co	10	12		13		16	41		40	16
Ni	10	18	22	16	18	21	34	90	91	8
Zn	53	56	57	56	59	65	76	78	80	74
Y	12	13	13	14	15	15	17	16	15	17
Zr	163	156	161	167	168	157	78	100	108	118
Nb	5·8	5·7	5·3	5·9	6·0	5·6	2·3	3·8	4·2	4·2
Ta	0·42	0·41		0·37		0·35	0·29		0·24	0·29
Hf	4·00	3·88		4·02		3·77	2·53		2·55	3·05
Th	8·39	7·93		7·39		6·48	1·90		2·52	3·24
Pb	16	16	16	14	14	13	7	9	8	11
La	20·1	19·9		20·0		19·1	12·4		13·0	14·7
Ce	42·8	42·6		42·7		40·7	30·7		26·3	31·8
Nd	17·9	18·5		19·2		19·2			13·3	15·3
Sm	3·32	3·35		3·63		3·73	3·85		3·36	4·08
Eu	0·87	0·88		0·96		0·99	1·24		1·05	1·32
Tb	0·42	0·40		0·45		0·45	0·54		0·41	0·54
Yb	1·28	1·30		1·44		1·37	1·45		1·44	1·57
Lu	0·20	0·20		0·22		0·21	0·21		0·21	0·23
$^{87}Sr/^{86}Sr$	0·703990	0·704006		0·704031		0·704026			0·704060	
2σ	0·000009	0·000010		0·000010		0·000010			0·000010	
Modes (vol. %; phenocrysts >0·3 mm; based on 1500 points, vesicle-free)										
Plagioclase	15·3	17·0		19·7	18·0	20·2	25·0	16·6	46·1	29·8
Olivine	0·1	0·6		0·6	0·9	1·0	5·0	7·5	10·2	0·1
Clinopyroxene	0·7	0·3		1·4	0·7	0·9	1·0	1·5	6·2	8·3
Orthopyroxene	0·5	1·0		0·9	1·0	1·2	0·1		2·1	0·1
Hornblende	3·8	1·4		tr	tr		5·0		3·7	0·1
Biotite	0·3	0·9		tr	tr					
Magnetite	1·2	0·8		0·5	1·0	0·7	0·5	0·4	2·8	2·4
Sum crystals	21·9	21·9		23·1	21·6	24·0	36·6	26·0	71·2	40·9

	Younger Holocene Lavas		Older Holocene Lavas			
	Summit lavas					
Map unit:	Qsp 1	Qsp 2	Qoh	Qoh	Qoh	Qoh
Sample:	PED-12	H-70	H-73	QH1-2	QH2-1	H-72
wt %						
SiO_2	55·5	56·7	55·4	54·8	53·9	62·2
TiO_2	1·02	1·01	1·11	1·04	1·02	0·62
Al_2O_3	18·03	17·70	18·35	18·73	18·03	17·84
FeO*	7·47	7·05	7·40	8·15	7·41	4·65
MnO	0·13	0·13	0·14	0·14	0·14	0·10
MgO	4·60	3·77	3·36	3·89	4·29	2·24
CaO	7·63	6·56	7·41	7·73	8·02	5·46
Na_2O	3·64	4·17	4·24	4·03	4·17	4·78
K_2O	1·36	1·65	1·41	1·36	1·31	1·63
P_2O_5	0·25	0·26	0·27	0·25	0·39	0·22
Total	100·5	99·7	99·9	100·1	99·5	100·3
Fe_2O_3	8·30	7·83	8·22	8·15	8·25	5·17
ppm						
Rb	35	46	34	32	33	38
Cs		1·8	1·4			
Sr	556	580	571	576	575	240
Ba	351	430	373	352	319	661
Sc	19·7	17·0	23·0			
V	181	142	195	34	178	15
Cr	77	23	9	20	39	b.d.
Co	45	24	22			
Ni	53	22	14	27	43	4
Zn	75	82	93	77	77	14
Y	18	17	20	19	19	13
Zr	111	147	144	138	136	128
Nb		6·0	5·6	4·1	4·0	4·9
Ta	0·30	0·33	0·26			
Hf	3·34	3·67	3·67			
Th	3·67	3·07	3·07			
Pb		12	10	9	10	10
La	15·4	17·7	16·0			
Ce	33·8	42·0	38·4			
Nd	17·0	21·0	20·2			
Sm	4·01	3·98	4·15			
Eu	1·21	1·31	1·40			
Tb	0·50	0·56	0·58			
Yb	1·55	1·56	2·10			
Lu	0·23	0·23	0·29			
$^{87}Sr/^{86}Sr$	0·704072	0·704109	0·704064	0·703952	0·704026	0·703921
2σ	0·000011	0·000010	0·000011	0·000011	0·000011	0·000011
Modes (vol. %; phenocrysts >0·3 mm; based on 1500 points, vesicle-free)						
Plagioclase	26·8	17·7	20·5		26·0	15·4
Olivine	2·0	1·6	0·2		0·7	
Clinopyroxene	2·3	0·1	0·1		1·0	0·5
Orthopyroxene		1·4	0·2		tr	0·8
Hornblende						
Biotite						
Magnetite	0·1	0·2			0·1	0·1
Sum crystals	31·2	21·0	21·0		27·8	16·8

*FeO estimated as 0·9 × Fe_2O_3.
b.d., below determination; tr, mineral present in very small amounts. (See text for methods and precision of the analyses.)

and c; Singer *et al.*, 1995; Feeley & Dungan, 1996) and lavas forming the Older Holocene portions of the composite Volcán San Pedro.

PETROGRAPHY AND MINERALOGY OF ERUPTIVE PRODUCTS

The Older Holocene lavas (samples H-73, QH1-2, QH2-1, H-72; Table 2) exhibit neither macroscopic nor microscopic evidence for mingling or mixing, nor is disequilibrium apparent among the phenocrysts. In contrast, the Younger Holocene lavas of the composite San Pedro flow (samples H-16, H-13, H-12, H-23, H-8, H-20; Table 2), for which we have obtained mineral compositions (Table 3), contain coarse-grained gabbroic xenoliths (Costa *et al.*, 2002), quenched basaltic inclusions (samples H-11i, H-8i, H-23i, H-20i; Table 2), and disequilibrium phenocryst assemblages (Singer *et al.*, 1995; Costa *et al.*, 2002). Electron microprobe analyses were acquired using a JEOL 733 instrument at Southern Methodist University operated at 15 keV and 20 nA with an electron beam of 5 μm width. Natural and synthetic mineral standards were used to monitor accuracy and precision, which are ~2–3% relative for the major oxides (Singer *et al.*, 1995).

Older Holocene lavas

The three basaltic andesite samples (H-73, QH1-2 and QH2-1) contain ~30% phenocrysts, and have porphyritic to seriate textures. Plagioclase is the predominant phenocryst, followed by clinopyroxene, orthopyroxene, and lesser olivine and Fe–Ti oxides (Table 2). The silicic andesite, H-72, has a seriate texture with 20% phenocrysts of plagioclase, clinopyroxene, orthopyroxene, and minor Fe–Ti oxides.

Younger Holocene eruptive products

Composite silicic lava flow

Dacitic to andesitic lavas forming the composite San Pedro flow are vitrophyric, with 22–24 vol. % phenocrysts (Table 2) set in pale grey to black glass. Plagioclase is by far the most abundant mineral either as a phenocryst (15–20 vol. %) or as microlites. Plagioclase compositions in the dacitic lavas define distinct modes at $An_{82–84}$, $An_{55–60}$, and $An_{45–50}$ (Fig. 4), whereas the andesite has also a population of anorthitic plagioclase and a less well-defined mode at ~An_{60}. Individual plagioclase phenocrysts in the silicic lavas typically exhibit repetitive normal zoning patterns ($An_{60–45}$) punctuated by dissolution surfaces that are correlated with abrupt shifts in major and trace elements (Singer *et al.*, 1995). These multiple normally zoned intervals are responsible for the modes at intermediate plagioclase compositions. The high anorthite population ($An_{82–84}$) consists of sieve-cored crystals, with textures and composition identical to those of the quenched basaltic inclusions, and thus these calcic crystals are probably xenocrysts derived from mechanical fragmentation of the quenched inclusions (Fig. 3; Singer *et al.*, 1995). In addition, numerous glomerophyric clots up to 1 cm diameter with phenocrysts up to 2 mm of calcic plagioclase (An_{80} cores mantled by An_{60} rims) + two pyroxenes + Fe–Ti oxides + glass are present in the Qcf 3 dacite.

The dacitic and andesitic lavas contain augitic clinopyroxene ($Wo_{40–46}$, $En_{41–44}$, $Fs_{13–16}$) and orthopyroxene ($Wo_{2–3}$, $En_{68–72}$, $Fs_{26–30}$); both pyroxenes show slight reverse (~3%) core to rim zoning in enstatite component in the Qcf 4 andesite. Fe–Ti oxides include titanomagnetite (XUlv$_{0·23–0·45}$) and rare ilmenite (XIlm$_{0·80–0·85}$). Using pairs of adjacent (but not touching) magnetite and ilmenite that fulfill the empirical Mg/Mn partitioning test for equilibrium (Bacon & Hirschmann, 1988) and the solution model of Ghiorso & Sack (1991), we estimated pre-eruptive crystallization temperature and oxygen fugacity for the Qcf 4 andesite and the Qcf 1 and Qcf 2 dacites. These are ~880–990°C near Ni–NiO for the andesite and a slightly lower range of temperature, ~840–930°C, but more oxidized, Ni–NiO + 1 log unit, for the dacites [Ni–NiO buffer of Heubner & Sato (1970)]. The large range in calculated crystallization temperature for each sample probably reflects the presence of Fe–Ti oxide xenocrysts from the basaltic inclusions. Hornblende- and biotite-bearing lavas are fairly scarce in the Southern Volcanic Zone (Hildreth & Moorbath, 1988) including the TSPC (Dungan *et al.*, 2001), thus the two most evolved dacite lava flows, Qcf 1 and Qcf 2, are unusual because they contain 1–4% of euhedral phenocrysts of both magnesiohastingsitic hornblende (Leake *et al.*, 1997) and biotite. The Al_2O_3 contents of hornblende vary from 6 to 10 wt % (Table 3), and the *mg*-number [= 100MgO/(MgO + FeO) in molecular proportions, where total iron is given as Fe^{2+}] from 62 to 71. The *mg*-number of biotite is 60–66 (Table 3). Trace amounts of hornblende and biotite rimmed by intergrowths of Fe–Ti oxides, orthopyroxene, and plagioclase are also present in the dacite Qcf 3, which contains up to 20 vol. % quenched inclusions of basalt (Fig. 3). We infer that breakdown of these hydrous minerals was caused by heating of the dacite that occurred before the eruption of this lava (e.g. Rutherford & Hill, 1993; see below). The andesite Qcf 4 does not contain hydrous minerals. Experiments on andesitic and dacitic compositions (e.g. Rutherford & Hill, 1993; Grove *et al.*, 1997; Scaillet & Evans, 1999) indicate that at least 4 wt % H_2O is necessary to stabilize hornblende, which constrains the pre-eruptive pressure of the dacitic magma to >1·5 kbar. Resorbed, or orthopyroxene-mantled olivine ($Fo_{82–69}$) is

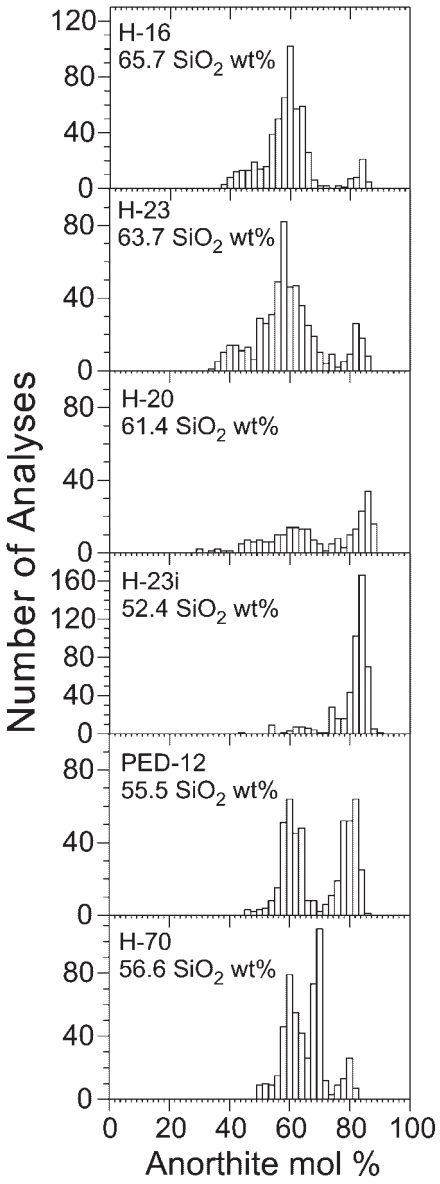


Fig. 4. Histograms of anorthite content of plagioclase phenocrysts in Younger Holocene lavas (samples H-16, H-23, H-20), a quenched basaltic inclusion (H-23i) of the composite flow, and the two summit-forming lavas (PED-12 and H-70). The tri-modal populations (at $An_{40–50}$, An_{60} and An_{82}) in the andesitic and dacitic lavas of the zoned flow should be noted. The anorthite frequency maxima at $An_{\sim 83}$ in these lavas match the maximum in the quenched basaltic inclusion H-23i and we interpret these anorthite-rich plagioclase crystals as xenocrystic and derived from fragmentation of the quenched inclusions. Similarly, the smaller plagioclase population in the inclusion H-23i at $An_{55–65}$ is interpreted as xenocrysts in the inclusions incorporated from the silicic host lavas. Summit-forming basaltic andesitic lavas PED-12 and H-70 contain mostly plagioclase with frequency maxima at about An_{80} and An_{60}, i.e. slightly less calcic than plagioclase in the quenched inclusion H-23i, but almost identical to the An_{60} peak of the dacites and andesites.

present in all silicic lava flows, but its proportion increases with decreasing silica content of the host lava (Table 2). These olivines are probably xenocrysts derived from mechanical fragmentation of the quenched basaltic inclusions (Singer *et al.*, 1995), which are described next.

Quenched basaltic inclusions

Rounded to irregularly shaped inclusions of quenched basalt (e.g. H8i, H23i; Table 2) up to 20 cm across (Fig. 3), some with vesiculated glassy rims, form 10–20% of various lobes of the Younger Holocene Qcf 3 dacite flow and contain calcic sieve-cored plagioclase, olivine ($Fo_{82–74}$), and augite phenocrysts ($Wo_{39–45}$, $En_{41–46}$, $Fs_{12–14}$) in a matrix of acicular plagioclase microlites and brown glass (Singer *et al.*, 1995). A far lesser volume of similar basaltic inclusions occurs in the Qcf 2 dacite (e.g. H-11i; Table 2). Microphenocrysts of orthopyroxene ($Wo_{2–3}$, $En_{65–73}$, $Fs_{24–32}$) and acicular hornblende are also present in the more crystal-rich inclusions. Plagioclase crystals are bytownite, $An_{80–85}$, with thin normal zoning at their rims. Some inclusions contain a small percentage of low anorthite plagioclase ($An_{55–65}$) displaying textural evidence of reaction by partial dissolution (e.g. Tsuchiyama, 1985), suggesting that these were incorporated into the mafic inclusion from the dacite host magma. Centimeter-sized, highly vesicular quenched inclusions of basaltic andesite (H-20i; Table 2) within andesite flow Qcf 4 consist of ~30 vol. % skeletal plagioclase, minor olivine, augite, magnetite, rare hornblende, and a matrix of pale brown glass.

Summit-forming basaltic andesitic lavas

The summit-forming basaltic andesite flows, Qsp 1 and Qsp 2 (samples PED-12 and H-70, respectively; Table 2), contain 32% and 21% phenocrysts of plagioclase, minor olivine, Fe–Ti oxides, and two pyroxenes. Clinopyroxene phenocrysts in flow Qsp 1 are rounded and resorbed ($Wo_{35–44}$, $En_{43–47}$, $Fs_{13–20}$). The latest summit-forming lava, Qsp 2, contains euhedral augite ($Wo_{42–45}$, $En_{41–45}$, $Fs_{12–15}$) and orthopyroxene (Wo_{3}, $En_{71–72}$, $Fs_{24–26}$). Most plagioclase crystals consist of a sieved bytownite core ($\sim An_{80}$) surrounded by an oscillatory zoned mantle of labradorite, $\sim An_{60}$, producing a bimodal population distribution (Fig. 4). The maximum An contents are slightly lower than the calcic xenocrysts of the silicic lavas or their quenched basaltic inclusions (Fig. 4). Olivine, mainly ranging from Fo_{73} to Fo_{68}, is less magnesian than that of the quenched basaltic inclusions or xenocrysts in the silicic flows.

MAJOR ELEMENT, TRACE ELEMENT, AND Sr ISOTOPE COMPOSITIONS

Analytical methods

Major and trace element compositions of freshly slabbed whole-rock samples (Table 2) were determined by X-ray

Table 3: Representative compositions (wt %) of selected minerals of Younger Holocene San Pedro lavas and magmatic inclusions

Mineral:	clinopyroxene				orthopyroxene		
Sample:	H-16	H-20	H-23i	PED-12	H-16	H-20	H-23i
Label:	cpx4-1r	cpx6-2r	cpx1-2r	cpx3-11r	opx2-1r	opx7-1r	opx2m
wt %							
SiO_2	50·96	50·62	51·62	52·11	53·56	53·55	53·41
TiO_2	0·43	0·68	0·69	0·69	0·36	0·20	0·32
Al_2O_3	1·80	2·88	2·49	2·10	0·99	1·42	1·88
FeO*	8·50	8·82	8·97	8·58	17·09	16·66	16·32
MnO	0·34	0·28	0·24	0·36	0·54	0·41	0·71
MgO	15·00	15·59	15·99	15·69	25·46	25·57	25·82
CaO	21·04	19·09	18·84	19·57	1·36	1·62	1·39
Na_2O	0·34	0·36	0·25	0·32	0·09	0·01	0·07
Sum	98·41	98·32	99·09	99·42	99·75	99·44	99·92
Wo	43·1	39·9	39·0	40·4	2·7	3·2	2·7
En	42·8	45·3	46·1	45·1	70·1	70·4	71·0
Fs	14·1	14·8	14·9	14·4	27·2	26·4	26·3
Mineral:	hornblende				biotite		
Sample:	H-16	H-16	H-13	H-13	H-16	H-13	H-13
Label:	hbl4-2	hbl3-3	hbl1-1	hbl4	bio6-1	bio1	bio1c
wt %							
SiO_2	48·80	44·40	41·78	44·77	37·16	36·48	37·35
TiO_2	0·96	1·99	2·90	2·04	3·70	3·72	4·00
Al_2O_3	5·88	9·71	11·19	9·4	13·57	13·49	13·71
FeO*	17·87	12·56	11·78	11·60	15·98	16·32	16·77
MnO	0·65	0·27	0·23	0·22	0·20	0·19	0·19
MgO	13·67	14·19	14·36	14·98	14·30	13·68	14·77
CaO	11·05	11·22	11·17	11·35	0·02	0·02	0·00
Na_2O	1·24	2·06	2·44	1·96	0·93	0·92	1·05
K_2O	0·34	0·50	0·40	0·52	8·42	8·93	8·95
BaO		0·05	0·04	0·04	0·62	0·54	0·39
F	0·34	0·11	0·05		0·10	0·02	
Cl	0·06	0·06			0·07	0·06	
F = O	0·14	0·05	0·02		0·04	0·01	
Cl = O	0·01	0·01			0·02	0·01	
Sum	97·70	97·06	96·32	96·88	95·01	94·32	97·18
mg-no.	62·1	66·8	68·5	69·7	61·5	59·9	61·1

*Total iron given as Fe^{2+}.
mg-number = 100MgO/(MgO + FeO), in molecular proportions, where total iron is given as Fe^{2+}.

fluorescence (XRF) at the University of Massachusetts and by instrumental neutron activation analysis (INAA) at the Massachusetts Institute of Technology following the methods described by Rhodes (1988) and Frey *et al.* (1990). Splits for XRF were crushed in tungsten carbide, whereas INAA splits were crushed in agate. The accuracy,

precision, and procedural blanks in these laboratories were established on the basis of replicate measurements of the BCR-1 standard (Frey *et al.*, 1990). Uncertainties in relative weight percentages for major oxides or ppm for trace elements at the 1σ level were estimated through replicate measurements of BCR-1 and for XRF are: SiO_2, 0·29; TiO_2, 0·25; Al_2O_3, 0·35; Fe_2O_3, 0·31; MnO, 2·93; MgO, 0·30; CaO, 0·23; Na_2O, 2·04; K_2O, 0·51; P_2O_5, 1·68; Rb, 3; Sr, 1; Ba, 3; Pb, 3; Zr, 1; Nb, 2; Cr, 3; Ni, 3; Y, 1; V, 2. Similarly, INAA uncertainties are: Cs, 3; Co, 2; Sc, 2; La, 2; Ce, 3; Nd, 4; Sm, 3; Eu, 2; Tb, 8; Yb, 3; Lu, 4.

Sr isotope compositions were determined at the University of California–Los Angeles using procedures of Feeley & Davidson (1994); nine measurements of the NBS-987 standard during this study gave a value of 0·710264 ± 7 (2 SEM). These, plus replicates of the unknown samples, resulted in an external precision of better than 7 ppm at the 2σ level for the Sr ratios in Table 2.

Older Holocene lavas

Older Holocene lavas comprise basaltic andesites containing 55 ± 1 wt % and a silicic andesitic lava with 62 wt % SiO_2 (Table 2; Fig. 5). Major, minor, and trace element concentrations and elemental ratios of the basaltic andesites are similar to those of the Younger Holocene mafic compositions, but with slightly higher Na_2O and lower MgO at a given SiO_2 content (Fig. 5). Older Holocene lavas range in $^{87}Sr/^{86}Sr$ from 0·70392 to 0·70406, with the most SiO_2-rich andesite having the lowest value (Fig. 6). Moreover, the andesite has lower K, Rb, and Sr concentrations and a lower $^{87}Sr/^{86}Sr$ ratio than the Younger Holocene andesitic to dacitic lavas (Figs 5 and 6). Older Holocene lavas are further distinguished in that they show remarkably limited ranges of K/Rb and Zr/Y compared with the Younger Holocene lavas and inclusions, despite having a larger range of $^{87}Sr/^{86}Sr$ ratios (Fig. 7). These trace element and Sr isotope differences suggest that Older and Younger Holocene magmas were derived from different sources.

Younger Holocene silicic lavas, quenched inclusions, and summit basaltic andesites

The composite San Pedro flow is chemically and isotopically zoned from high-K calc-alkaline dacite with 65·8 wt % SiO_2 and $^{87}Sr/^{86}Sr$ of 0·703990 to andesite with 61·4 wt % SiO_2 and $^{87}Sr/^{86}Sr$ of 0·704026 (Figs 5 and 6; Table 2). Quenched basaltic inclusions, containing 51·5–52·5 wt % SiO_2 and 5·9–7·4 wt % MgO, in the Qcf 3 dacite extend the $^{87}Sr/^{86}Sr$ variation of the zoned eruption to 0·704060, a value that is higher than any for the Qcf lavas (Fig. 6). Younger basaltic andesites that constitute the flank (55·5 wt % SiO_2) and summit (56·7 wt % SiO_2) of Volcán San Pedro have $^{87}Sr/^{86}Sr$ of 0·704072 and 0·704109, respectively, within the range of the quenched inclusions, but higher than values of the andesitic and dacitic lavas (Fig. 6). The composite San Pedro flow and the summit-forming basaltic andesites display collinear trends in major and trace elements (Figs 5 and 6). In contrast, the quenched basaltic inclusions in the Qcf 3 dacite are not collinear with the Younger Holocene lavas for major elements including Al_2O_3, P_2O_5, and MgO (Fig. 5). It should be noted that the quenched inclusions (H-20i, Table 2) in the Qcf 4 andesitic lava are virtually indistinguishable in major and trace element composition from the younger summit-forming Qsp 2 lava (Figs 5 and 6), suggesting that the later summit-forming basaltic andesite magma resided in the same magma reservoir as the silicic magmas that erupted to form the zoned composite flow.

Concentrations of Rb, Zr, La, and Th in general increase with SiO_2, whereas Y, Yb, Sr, and Ni decrease (Fig. 6). Ratios of incompatible elements Zr/Y and La/Yb increase linearly with Rb, whereas K/Rb and $^{87}Sr/^{86}Sr$ ratios decrease (Fig. 7). Although the range of incompatible trace element and Sr isotope ratios is small, they vary together in a systematic way that precludes simple fractional crystallization as the mechanism that generates the andesitic and dacitic magmas from either the quenched inclusions or the summit basaltic andesite. As we will show below, the compositional and isotopic zoning of the silicic lavas are best explained by mixing different proportions of the most evolved dacite with the summit-forming basaltic andesite.

Late Pleistocene Guadal and Tatara dacites

Whereas rhyolite is exceedingly rare in the TSPC, small volumes of dacitic magma (63–68 wt % SiO_2) possessing contrasting geochemical, mineralogical and textural characteristics were erupted at various times (Singer *et al.*, 1995, 1997; Dungan *et al.*, 2001). To illustrate these contrasts and place the origin of the Younger Holocene San Pedro dacite into a temporal frame of changing subvolcanic processes over the last several hundred thousand years, we briefly describe chemical compositions of the Guadal (~350 ka; Feeley & Dungan, 1996; Feeley *et al.*, 1998) and Tatara (68 ka; Singer *et al.*, 1995) dacites, both of which crop out on the flanks of Volcán San Pedro (Fig. 2a and c). The Guadal dacites contain abundant quenched mafic inclusions, indicating that mingling and mixing of magmas were important processes (Feeley & Dungan, 1996). They contain 66–67·5 wt % SiO_2 with the least silicic compositions having slightly

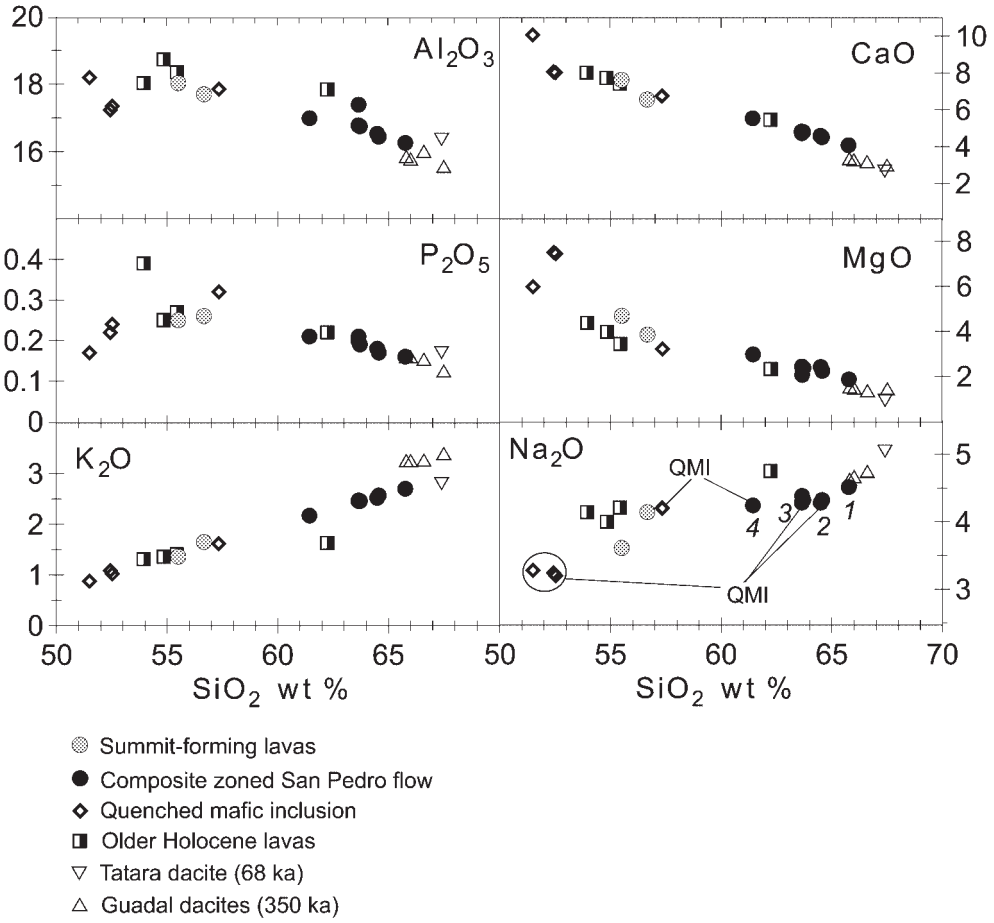


Fig. 5. Major element Harker diagrams (concentrations in wt %) for the Holocene lavas and quenched inclusions. For comparison, Tatara (68 ka) and Guadal (350 ka) dacites are also plotted. In the Na_2O vs SiO_2 diagram the numbers indicate the sequence of eruption of the composite flow and the lines relate the quenched inclusions to their host lavas.

higher K_2O and lower MgO and CaO than the San Pedro dacite H-16 (Fig. 5). Relative to the Younger Holocene San Pedro dacite, Guadal dacites contain more Rb, La, Th, Zr, and Y, and lower Sr, yet the Sr is slightly more radiogenic (Fig. 6). Although Guadal dacites have K/Rb and Zr/Y ratios remarkably similar to those of San Pedro dacite, their La/Yb, Sr/Y, and Ba/Y ratios are much lower (Fig. 7). Feeley *et al.* (1998) proposed that Guadal dacites originated by partial melting of gabbroic crustal rocks at 3–7 kbar and subsequent crystallization and mixing with basaltic andesitic magma. The contrasts in $^{87}Sr/^{86}Sr$, La/Yb, Sr/Y, and Ba/Y ratios indicate that the source rocks or processes that produced the Younger Holocene San Pedro dacite were different from those responsible for the Guadal dacites (see Discussion).

In contrast to the Guadal and San Pedro dacites, the Tatara dacite (67·5 wt % SiO_2) is phenocryst poor and displays no evidence for mingling or mixing with mafic magma (Singer *et al.*, 1995). Ferguson *et al.* (1992) proposed an assimilation–fractional crystallization origin from a basaltic andesite parent magma. The Tatara dacite is collinear with San Pedro major element variations (Fig. 5) and contains amounts of Ni and Th similar to the most evolved San Pedro dacite (Fig. 6). However, the Tatara dacite has much higher La, Y, and Zr, and slightly lower Rb and Sr contents than the San Pedro dacites (Fig. 6). The Tatara dacite also has a lower La/Yb, Sr/Y, Ba/Y, and Zr/Y, and higher K/Rb ratio than the San Pedro dacites (Fig. 7). The $^{87}Sr/^{86}Sr$ ratio, 0·704060, of the Tatara dacite is indistinguishable from that of the San Pedro dacite, but slightly lower than for the Guadal dacite (Fig. 6). The mineralogical, textural, trace element, and isotopic differences between these evolved magmas point to multiple magma sources and shifts in differentiation processes over the past ~350 kyr.

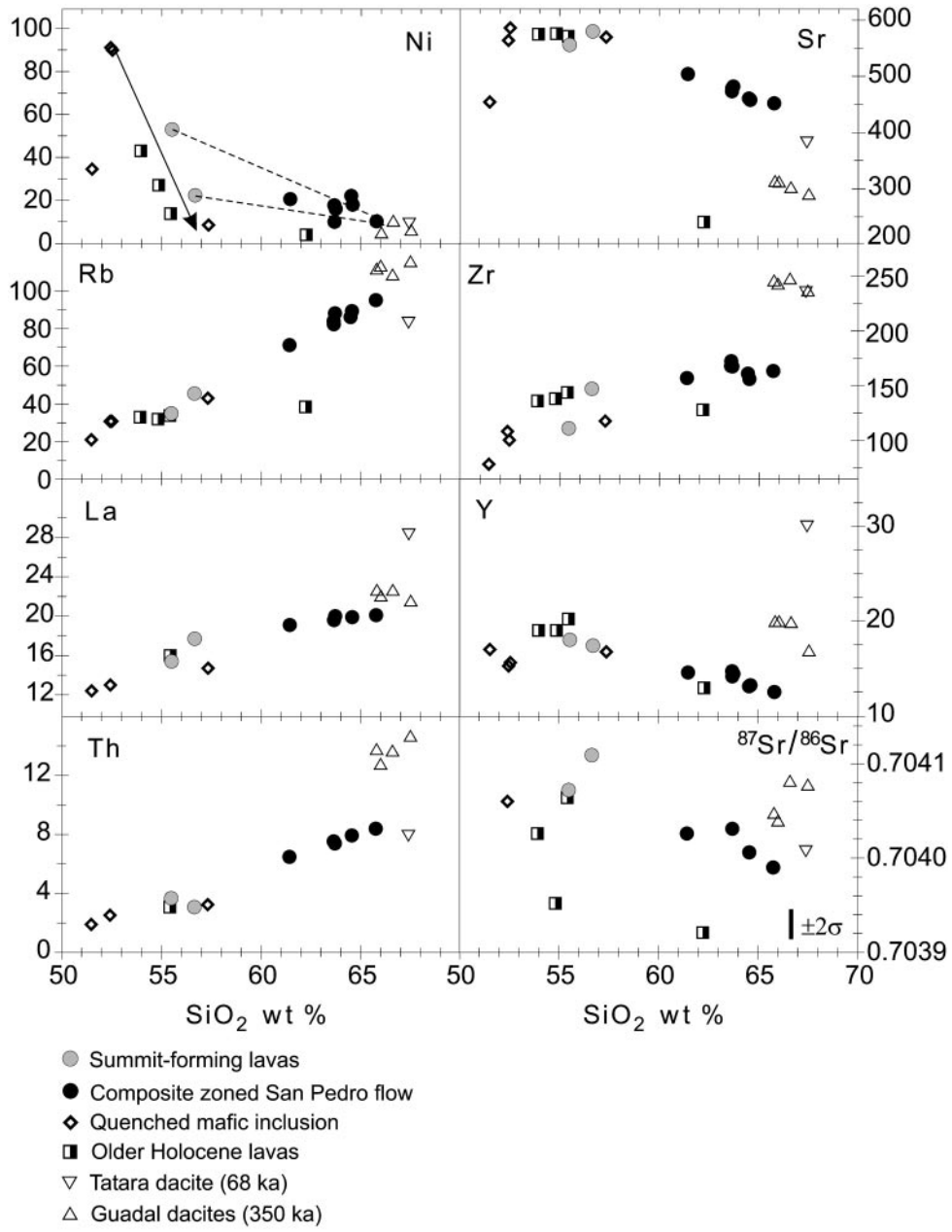


Fig. 6. Trace element (concentration in ppm) and Sr isotope variation diagrams for the Holocene lavas, quenched inclusions, and Tatara (68 ka) and Guadal (350 ka) dacites. Arrow in the Ni vs SiO_2 diagram illustrates fractionation of olivine + plagioclase + clinopyroxene + magnetite from basalt to generate basaltic andesite. Dashes lines show mixing trends from the basaltic andesites to the dacites. It should be noted that the silicic Holocene lavas do not fall exactly on the mixing lines because of the effect of mingling, i.e. selective incorporation of forsteritic olivine with high Ni contents.

DISCUSSION

Origin of compositional zoning in the Younger Holocene San Pedro magma chamber

Compositional zoning in silicic systems has been observed in a number of eruptions (see references in the Introduction). The origin of such zoning has been ascribed to two main processes: (1) crystal fractionation including side-wall crystallization whereby less dense evolved liquids migrate towards the upper parts of the chamber, producing a gravitationally stable stratification (e.g. Turner & Gustafson, 1981; McBirney *et al.*, 1987; Bacon & Druitt, 1988; (2) incomplete mixing after

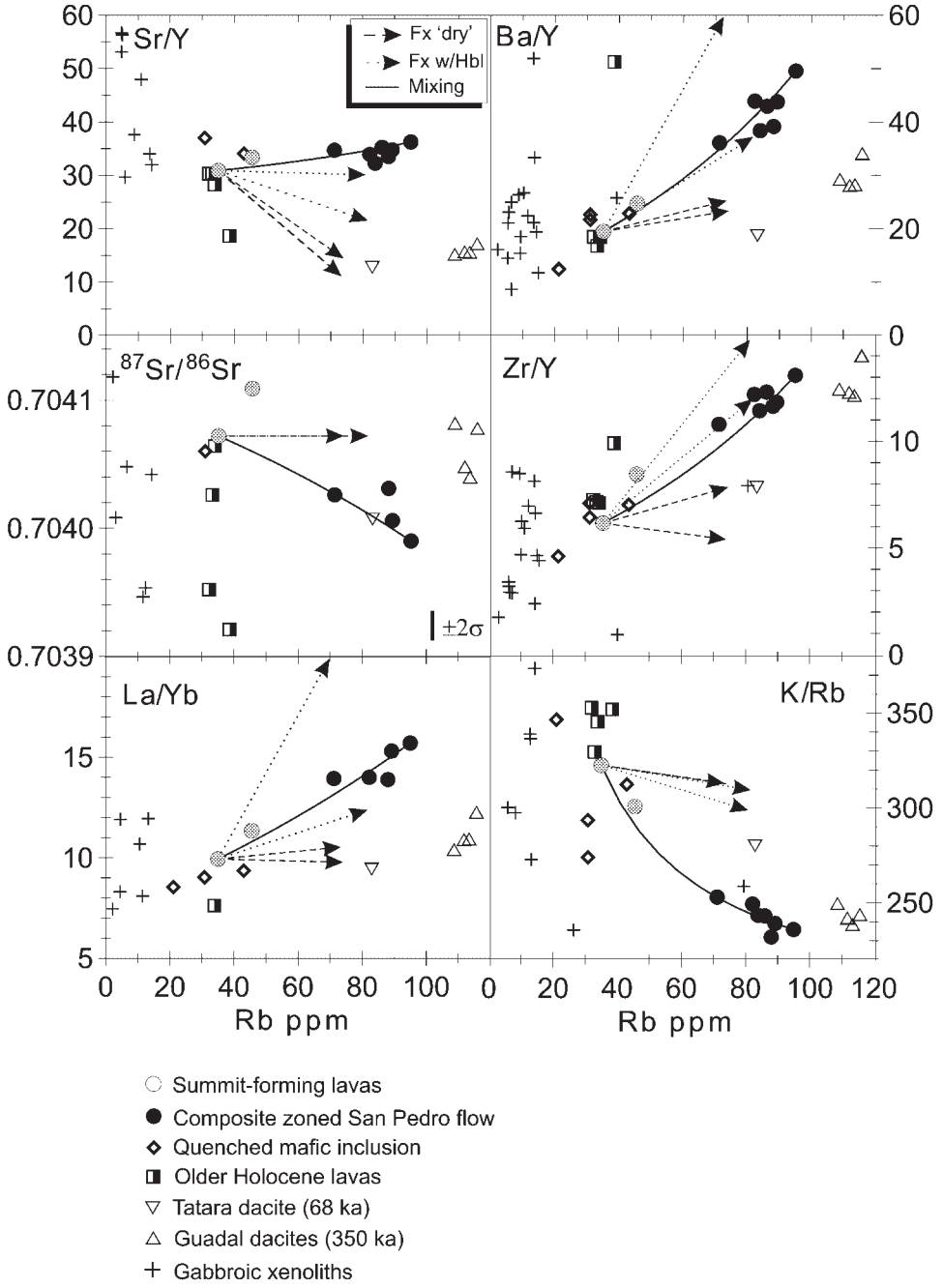


Fig. 7. Trace element and Sr isotope ratio variation diagrams for the Holocene lavas, quenched inclusions, and gabbroic xenoliths (some xenoliths with extreme trace element ratios are not shown; Costa *et al.*, 2002). For comparison, Tatara (68 ka) and Guadal (350 ka) dacites are also plotted. Continuous line shows mixing trend between basaltic andesite PED-12 and San Pedro dacite H-16 and reproduces most geochemical features of the lavas in the composite San Pedro flow. Arrows delineate models of anhydrous or amphibole-bearing mineral assemblages fractionated from a basaltic andesite parent. Mineral proportions constrained by major element mass balance (see Table 4); diverging arrows in both models reflect a range of partition coefficients (Appendix, Table A1).

intrusion of an unrelated silicic or mafic magma into the chamber (e.g. Snyder & Tait, 1998; Eichelberger *et al.*, 2000). The silicic lavas of the Younger Holocene eruption show extensive field, mineralogical and geochemical evidence for mingling and mixing, and thus hybridization of silicic and mafic magmas is likely to be responsible for the major and trace element and Sr isotope zoning of these lavas.

The andesite Qcf 4 contains 61·4% SiO_2 and lies intermediate and collinear in major and trace element

Table 4: Mass-balance calculations for major element fractionation models of Younger Holocene San Pedro lavas and quenched inclusions

Model:	(1) Basalt to basaltic andesite						(2) Basaltic andesite to dacite (anhydrous)						(3) Basaltic andesite to dacite (hydrous)			
	P	D	C	R	S.M. (wt %)		P	D	C	R	S.M. (wt %)		C	R	S.M. (wt %)	
Sample:	H-23i	PED-12					PED-12	H-16								
SiO_2	52·8	55·7	55·6	0·10	Ol (Fo_{80})	8·0	55·7	66·0	65·9	0·17	Ol (Fo_{70})	7·9	65·9	0·11	Opx	7·9
TiO_2	1·0	1·0	1·0	0·00	Cpx	3·4	1·0	0·5	0·9	0·43	Cpx	5·6	0·6	0·11	Hbl	12·4
Al_2O_3	17·4	18·1	18·0	0·07	Pl (An_{70})	11·1	18·0	16·3	16·3	0·03	Pl (An_{60})	35·2	16·4	0·06	Pl (An_{60})	34·3
FeO*	8·5	7·5	7·4	0·08	Mt	1·3	7·5	3·8	3·6	0·16	Mt	3·7	3·6	0·14	Mt	3·4
MnO	0·2	0·1	0·2	0·05			0·1	0·1	0·1	0·05	Ap	0·4	0·2	0·10	Ap	0·4
MgO	7·5	4·6	4·6	0·04			4·6	1·8	1·8	0·01			0·04			
CaO	8·1	7·7	7·6	0·02	*F*	23·8	7·7	4·1	4·1	0·01	*F*	52·8	3·8	0·25	*F*	58·5
Na_2O	3·3	3·7	3·8	0·17			3·7	4·6	4·3	0·24			0·15			
K_2O	1·1	1·4	1·4	0·05	R^2	0·06	1·4	2·7	2·8	0·11	R^2	0·32	3·1	0·34	R^2	0·26
P_2O_5	0·2	0·3	0·3	0·04			0·3	0·2	0·2	0·00			0·2	0·00		

*Total iron given as Fe^{2+}.
Model 3 uses the same parent and daughter compositions as model 2. P, parent; D, daughter; C, calculated; S.M., subtracted minerals; *F*, amount of crystallization; *R*, residual; R^2, sum of the square of the residuals; Pl, plagioclase; Ol, olivine; Cpx, clinopyroxene; Opx, orthopyroxene; Hbl, hornblende; Mt, magnetite; Ap, apatite.

composition between the most silicic dacite Qcf 1 with 65·8% SiO_2 and the subsequently erupted basaltic andesite Qsp 1 having 55·5% SiO_2 (Figs 5 and 6), and contains heterogeneous crystal populations that vary widely in composition, zoning patterns, and textures (e.g. Fig. 4). Its temporal and spatial position strongly suggests that it resided below the dacitic magmas in the zoned chamber and was above the succeeding basaltic andesite of the early summit-forming eruptions. Accordingly, we have tested the hypothesis that mixing played a major role in the compositional zoning observed in the silicic lavas through major element mass-balance calculations. Mixing 42% of the basaltic andesite PED-12 and 58% of the most evolved H-16 dacite reproduces the H-20 andesite with low residuals (R^2 = 0·13; Fig. 8). Modeling of the trace elements and $^{87}Sr/^{86}Sr$ ratios using mixing proportions that fulfill the major element constraints also reproduces the andesitic composition remarkably well (Figs 7 and 8). The fact that all silicic lavas contain olivine and plagioclase xenocrysts, or quenched basaltic inclusions, different in composition from the summit-forming basaltic andesites, points toward a more complex history than the simple mixing scenario proposed above, however. As the highest anorthite and forsterite contents of plagioclase and olivine xenocrysts are like those of the quenched basaltic inclusions, the silicic lavas also preserve a record of intricate mingling with a magma more magnesian and calcic than the PED-12 composition—a magma akin to that forming the quenched basaltic inclusions. The major element composition of these inclusions, however, precludes this basalt from being the mafic mixing end-member in the origin of the andesite. To reconcile these observations, it is useful to consider thermo-mechanical relations of the mafic and silicic end-members (e.g. Bacon & Metz, 1984; Bacon, 1986; Sparks & Marshall, 1986).

Forceful injection of small quantities of ~1100°C basalt into voluminous cooler ~ 900°C dacite magma would quench the basalt in small blobs (e.g. Fig. 3) and would limit the interactions between the two magmas (e.g. Bacon, 1986; Sparks & Marshall, 1986; Campbell & Turner, 1989). The possibility of mixing by mechanical blending and chemical diffusion is greatly enhanced if the proportions of mafic and silicic magma are subequal and their compositions are such that upon thermal equilibration both end-members remain at least partially molten (e.g. Sparks & Marshall, 1986; Oldenberg *et al.*, 1989). We propose that following initial injection of basalt into the dacite rapid cooling of the basalt against the dacite led to its crystallization and fractionation to a basaltic andesite composition. Using the composition of the quenched basaltic inclusion H-23i as parent and the PED-12 basaltic andesite as daughter, subtraction of ~24 wt % of a mineral assemblage consisting of 8 wt % of olivine (Fo_{80}), 3·4 wt % of clinopyroxene, 11 wt % of plagioclase (An_{70}), and 1·3 wt % of Fe–Ti oxides, produces a composition like the basaltic andesite with low residuals (Table 4). Upon differentiating to a composition similar to PED-12, the two magmas reached thermal equilibrium, yet remained sufficiently molten to begin mixing in the proportions modeled above. The small quantity of quenched inclusions of basaltic andesite (H-20i; Table 2) in the Qcf 4 andesite lava is a tangible vestige of the mafic end-member that participated in this mixing process.

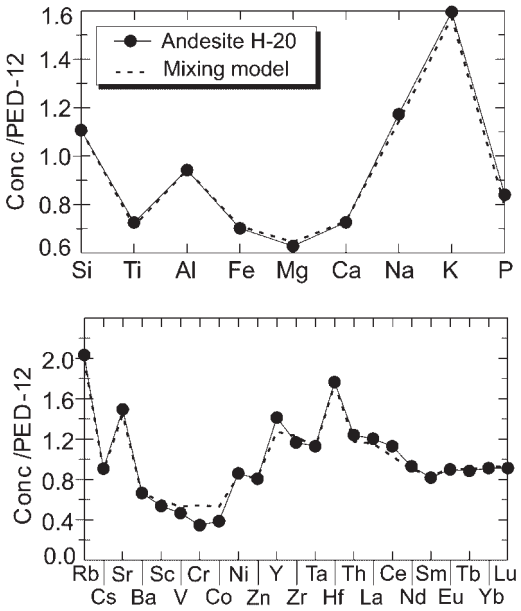


Fig. 8. Major and trace element mixing models for the origin of the H-20 andesite. Mixing 42 wt % of basaltic andesite PED-12 and 58 wt % of the most evolved dacite H-16 produces compositions like those of the andesite with R^2 of 0·1.

Thermal conduction of heat from the basaltic andesite into the dacite would certainly have raised the temperature of the hybrid andesite and possibly devolatilized the hybrid magma to conditions outside the stability of hornblende and biotite, which are absent in the Qcf 4 andesite and probably completely resorbed. A much larger volume of dacite overlying the hybrid andesite magma was probably also heated to a lesser degree; in this part of the chamber hornblende and biotite became unstable and although most crystals were dissolved or reacted to form orthopyroxene + oxide + plagioclase intergrowths, a few relict hornblende crystals survived (Fig. 3d). Moreover, heating of the dacitic magma from below by the cooling basalt would have promoted thermal buoyancy and possibly convective mixing (e.g. Oldenburg *et al.*, 1989). We have proposed that thermal changes associated with convective cycling were responsible for the repetitive cycles of $An_{45–50}$ plagioclase dissolution and An_{60} growth, forming oscillatory zoned crystals with

anorthite-rich peaks associated with high Mg, Fe, and Sr concentrations in most of the dacites (Fig. 4, and see Singer *et al.*, 1995).

Origin of the dacite magma: fractional crystallization vs partial melting of phlogopite-bearing gabbros

Several petrological and compositional features of the most evolved dacite Qcf 1 are remarkable in the context of the Holocene lavas and also in the entire TSPC: (1) it is among the rare lavas that contain both biotite and hornblende phenocrysts; (2) it has higher La/Yb (~15), Sr/Y (~36), and Ba/Y (~50) than any other dacite of the TSPC; (3) its Sr/Y values are similar to the Holocene mafic compositions, but its La/Yb, Ba/Y are much higher, whereas the K/Rb are much lower; (4) its $^{87}Sr/^{86}Sr$ ratio, 0·70399, is among the lowest of the TSPC. In the discussion below we test the alternative hypotheses that this dacite is the product of (1) fractional crystallization of mafic magma (plus minor assimilation) or (2) partial melting of gabbro. We propose that dehydration partial melting of phlogopite-bearing gabbroic rocks similar to those found as xenoliths in the San Pedro dacite provides the most plausible explanation for the high Ba/Y and Sr/Y ratios, and low K/Rb and $^{87}Sr/^{86}Sr$ values of the dacite.

Fractional crystallization models

Derivation of the dacite from a mafic parent by crystal fractionation was tested first by mass-balance calculations (Table 4). For these, we used the basaltic andesite composition of PED-12 as parent magma and the mineral compositions determined by electron microprobe. PED-12 was chosen as a parent because it is (1) the most SiO_2-poor, MgO-rich lava that erupted during the Younger Holocene, (2) similar in composition to basaltic andesite that erupted during the preceding Older Holocene period (Figs 5 and 6), and (3) typical of basaltic andesitic lavas, which make up the vast majority of the TSPC (Singer *et al.*, 1997; Dungan *et al.*, 2001). Subtraction of ~53 wt % of an assemblage comprising ~8 wt % olivine (Fo_{70}), 5·6 wt % clinopyroxene, 35·2 wt % plagioclase (An_{60}), 3·7 wt % Fe–Ti oxides, and 0·4 wt % apatite produced a liquid resembling the dacite (H-16) with low residuals ($R^2 = 0·3$). Rayleigh crystallization trace element modeling using this assemblage and partition coefficients from the literature (Appendix, Table A1) produces compositions unlike the dacite; most notably they have lower incompatible element abundances (e.g. Rb), much lower Sr/Y, Ba/Y, and La/Yb, and much higher K/Rb (Fig. 7). Consequently, differentiation of typical mafic magma through crystallization of an anhydrous assemblage is an unlikely origin for the dacite. In contrast, some features of the Tatara dacite (e.g. Sr/Y, Ba/Y, La/Yb) are explained by crystallization of an anhydrous mineral assemblage from a parent magma similar to PED-12, although its K/Rb value suggests that some open-system crystallization may have occurred (Ferguson *et al.*, 1992).

To further explore whether the San Pedro dacite can be derived by fractional crystallization from a mafic parent, we have tested the possibility that hornblende was a crystallizing mineral, as hornblende phenocrysts are present in all dacitic lavas. Mass-balance calculations using the PED-12 basaltic andesite as a parent produce compositions like the dacite, and require ~58 wt % crystallization of the assemblage 7·9 wt % orthopyroxene, 12·4 wt % hornblende, 34·3 wt % plagioclase (An_{60}), 3·4 wt % Fe–Ti oxides, and 0·4 wt % apatite (Table 4). With respect to the dacite, Rayleigh crystallization of this mineral assemblage produces compositions with lower incompatible element abundances (e.g. Rb), but comparable Sr/Y, Ba/Y, and La/Yb ratios. However, the K/Rb of the calculated composition exceeds the low value observed in the dacite, which could be matched only if crystallization was accompanied by assimilation of low K/Rb material. PED-12 has a K/Rb ratio of 325, placing it among the lowest of several hundred basaltic and basaltic andesitic lavas measured from within the TSPC, of which virtually all that are younger than 350 ka have K/Rb between 600 and 300 (Dungan *et al.*, 2001). Thus, were we to test additional parent magma compositions that might be considered more representative of the TSPC, we would choose parents with K/Rb values much higher than PED-12, none of which are capable of producing the low K/Rb values of the Younger Holocene dacite through crystallization alone.

Assimilation of silica-rich rocks, or partial melts derived from them, for example the Miocene granitoid plutons that form part of basement of the TSPC (Fig. 2), could lower the K/Rb values significantly, as these granitoids have high Rb contents (200–280 ppm) and low K/Rb (140–200; Nelson *et al.*, 1999). However, these plutons are characterized by $^{87}Sr/^{86}Sr$ values higher than 0·7041 (Fig. 9a) and thus assimilation would tend to produce magmas more radiogenic than the dacite. Moreover, the granitoids have lower Ba/Y (<42) and much lower Sr/Y (<22) so that their assimilation would lower these ratios, producing magmas different from the San Pedro dacite. We next turn to partial melting of hornblende- and phlogopite-bearing gabbroic rocks akin to the observed xenoliths as a possible origin of the San Pedro dacite.

Partial melting of hornblende- and phlogopite-bearing gabbro

Partial melting of hydrous gabbroic rocks has been cited as a mechanism to generate silicic magma in a number

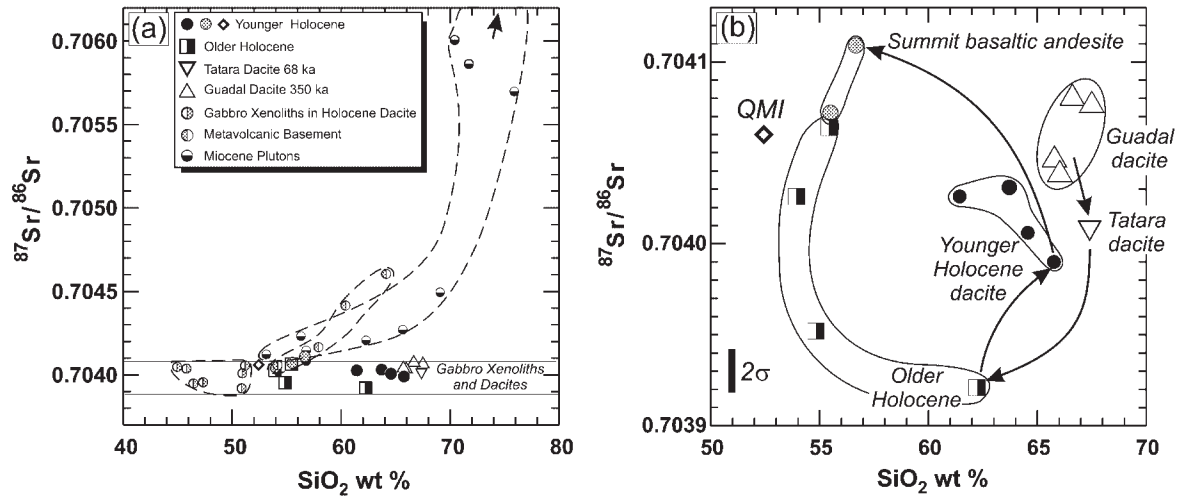


Fig. 9. $^{87}Sr/^{86}Sr$ ratios vs SiO_2 contents for lavas, exposed Tertiary basement rocks, and gabbroic xenoliths at Volcán San Pedro. (a) Comparison of lavas with local Miocene granitoid plutons, metavolcanic rocks, and hornblende–phlogopite gabbroic xenoliths found in the younger Holocene Qcf 2 dacite. The ranges of $^{87}Sr/^{86}Sr$ ratios of the lavas and the gabbroic xenoliths (0·7039–0·7041) are identical, whereas the values for the basement rocks are generally >0·7041. Data sources: Guadal dacite, Feeley *et al.* (1998); Tatara dacite, J. Davidson (unpublished data, 1995); Miocene granitoid plutons and metavolcanic rocks, Nelson *et al.* (1999); gabbroic xenoliths from San Pedro Qcf 2 lava, Costa (2000). (b) Arrows illustrate changes in the $^{87}Sr/^{86}Sr$ of the most silicic lavas erupted during the four volcanic episodes of the last 350 kyr. QMI, quenched mafic inclusions.

of settings (e.g. Mount St. Helens dacite, Smith & Leeman, 1987; Chilliwack Batholith, Tepper *et al.*, 1993; Guadal dacite, Feeley *et al.*, 1998). Unfortunately, modeling of partial melting is far less well constrained than fractional crystallization, in part because one must infer the assemblage and proportions of residual minerals, which are rarely sampled. A common approach is to use the modes produced during experiments that partially melted mafic rocks (e.g. Beard & Lofgren, 1991; Sen & Dunn, 1994; Wolf & Wyllie, 1994; Rapp & Watson, 1995). The gabbroic xenoliths found in the Younger Holocene San Pedro dacite flow Qcf 2 (Costa *et al.*, 2002) are characterized by large amounts of modal hornblende (to 50%) and phlogopite (to 28%) and display a large range of trace element abundances and ratios (e.g. Rb = 3–80 ppm, K/Rb = 170–630, Ba/Y = 10–70, La/Yb = 7–12; Fig. 7). Moreover, these xenoliths have relatively low $^{87}Sr/^{86}Sr$ values identical to those of the San Pedro dacite (Figs 7 and 9a). We modeled partial melting using as protoliths two gabbroic xenoliths described by Costa *et al.* (2002) that comprise variable proportions of modal plagioclase (~25–50%), hornblende (~25–50%), orthopyroxene (8–10%), and phlogopite (~3–4%), and with different abundances and ratios of trace elements (Fig. 10).

To constrain the mineral modes and degree of melting we used the 3 kbar dehydration and water-saturated experiments of Beard & Lofgren (1991) on a hornblende hornfels (their sample 466) that is mineralogically and compositionally similar to the San Pedro gabbroic xenoliths. In the dehydration experiments, 20–30% melting at 900–1000°C produced dacitic to rhyolitic glasses, leaving a residuum of mainly plagioclase (~55 wt %) and clinopyroxene (~25 wt %). Water-saturated conditions required higher degrees of melting, 30–45%, but lower temperatures, 900–950°C, to produce dacitic to rhyolitic glasses, and a residuum containing ~25 wt % hornblende. Trace element modeling using a batch melting equation produces melts with lower concentrations of Rb than the San Pedro dacite, but Sr/Y, Ba/Y, Zr/Y, and K/Rb values that partly overlap it, depending on the protolith and conditions of melting (Fig. 10). Calculated dehydration melts from both protoliths have Sr/Y and Ba/Y that are more similar to those of the San Pedro dacite than melts produced under water-saturated conditions, consistent with partial melting under low water contents. In contrast, the melting conditions appear to have less influence on the Zr/Y and K/Rb values than does the initial composition of the protolith. For example, melts calculated using the Hx14z xenolith as a protolith better explain the high Zr/Y, and particularly the low K/Rb values of the San Pedro dacite (Fig. 10).

Low K/Rb values relative to most gabbroic xenoliths and basaltic to basaltic andesitic lavas of the TSPC are characteristic not only of the San Pedro dacite, but also the older Guadal dacite (Fig. 10). If these dacites were indeed derived through extensive melting of gabbroic rocks, as had been proposed for the Guadal dacite (Feeley

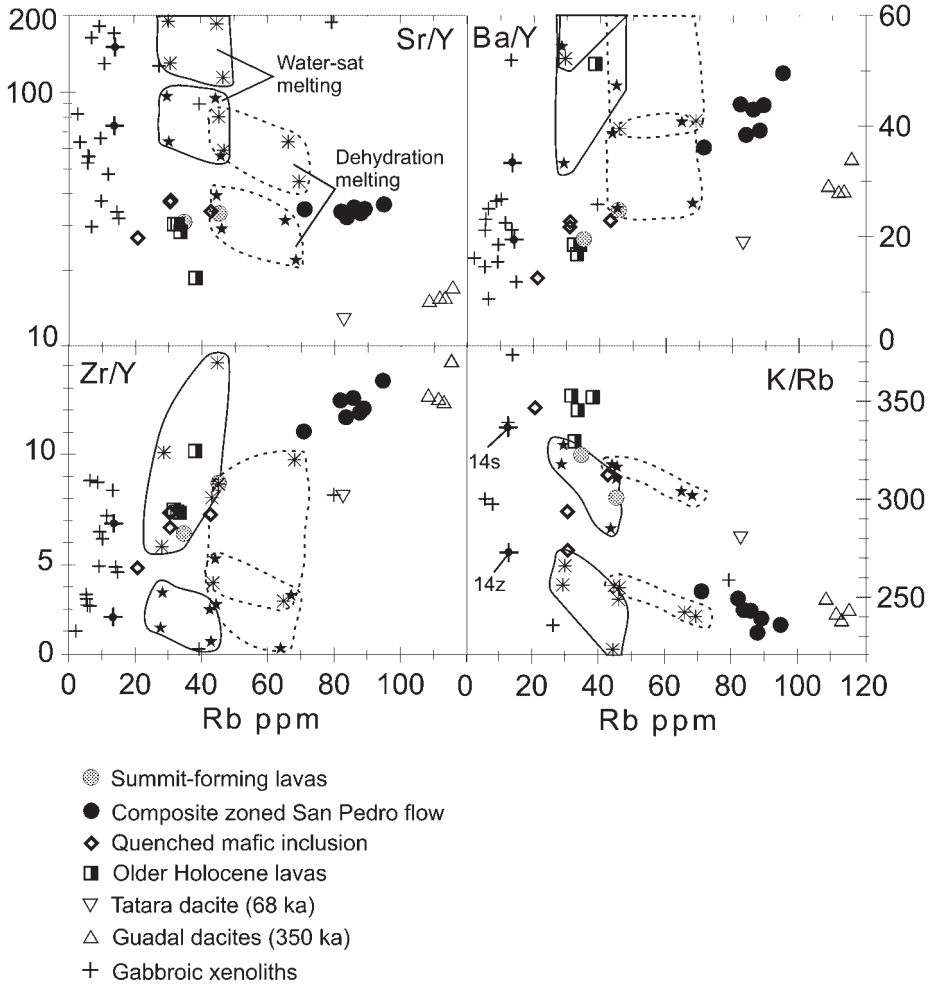


Fig. 10. Trace element ratios vs Rb contents for the Holocene lavas, quenched inclusions, Tatara and Guadal dacites, and gabbroic xenoliths of Costa *et al.* (2002). Model compositions from the partial melting of two of the gabbroic xenoliths (samples Hx14s and Hx14z, denoted as crosses with filled circles) calculated using the residual mineral modes of dehydration and water-saturated experiments at 3 kbar of Beard & Lofgren (1991; their starting composition 466, charges 113, 158, 144, and 164). The calculated compositional ranges reflect the contrasting extent of melting in the charges, plus the range of possible partition coefficients (Appendix, Table A1).

et al., 1998), their low K/Rb values most probably reflect low K/Rb in the protoliths. In gabbroic xenoliths studied by Costa *et al.* (2002), the budgets of K and Rb are controlled by the proportion of modal phlogopite. For instance, we have calculated the K/Rb values of phlogopite in the gabbroic xenoliths by using their K_2O concentration measured by electron microprobe (~8·5 wt %; Costa *et al.*, 2002) and assuming that all Rb in the whole rock resides in phlogopite. Mass-balance calculations using the three xenoliths that have the highest modal proportions of phlogopite (~10–30%; Costa *et al.*, 2002) yielded 280–333 ppm Rb in phlogopite, and in turn K/Rb values of 212–256, which overlap those of the bulk rock (K/Rb = 170–260). Thus, partial melting of relatively young (<Miocene) gabbroic rocks, similar to the xenoliths that contain abundant hornblende and phlogopite, may be an underappreciated, yet important, mechanism in generating dacitic lavas at the TSPC, particularly those like the Guadal and San Pedro dacites distinguished by low K/Rb and $^{87}Sr/^{86}Sr$ ratios (Fig. 9a).

The evolving magmatic system beneath Volcán San Pedro

Eruptions over the past 930 kyr at the TSPC reflect the arrival of many batches of mafic magma in the subvolcanic plumbing system that (1) crystallized, mixed, and assimilated crust (Singer *et al.*, 1997; Dungan *et al.*,

2001) and (2) occasionally promoted intracrustal melting (Feeley *et al.*, 1998; this study). Neither the exact sequence of magmas nor details of their genesis have emerged, yet this information is essential to constrain rates of melting, crystallization, mixing, and magma ascent, which in turn govern eruptive hazards at arc volcanoes (Hobden *et al.*, 1999; Turner *et al.*, 2000). Mineralogy, trace element contents, and Sr isotope ratios point to the presence of at least six distinct magmas beneath Volcán San Pedro at various times during the last 350 kyr. The Guadal dacite is a hydrous crustal melt that contained amphibole and quenched inclusions of basalt (Feeley & Dungan, 1996) thereby reflecting the coexistence of both basaltic and silicic magma at 350 ka. In contrast, the 68 ka Tatara dacite contains rare resorbed amphibole, no basaltic inclusions, and probably evolved through fractional crystallization of basaltic andesite (Singer *et al.*, 1995). Older Holocene lavas contain no amphibole, biotite, or basaltic inclusions, but encompass an unusual range of trace element and $^{87}Sr/^{86}Sr$ ratios that preclude a relationship by fractional crystallization; assimilation of relatively unradiogenic crust, as sampled by the gabbroic xenoliths (Fig. 9a), seems likely. We have presented evidence that Younger Holocene magmatism reflects partial melting of gabbro to produce amphibole- and biotite-bearing dacitic magma and that mingling and limited mixing of the dacite with basalt created a strongly zoned magma body. Subtle differences in trace element and $^{87}Sr/^{86}Sr$ ratios (Fig. 9b) between the Guadal dacite, Older Holocene andesite, and San Pedro dacite suggest that contrasting crustal domains or melting behavior participated with each new influx of mafic magma into the subvolcanic plumbing system. Simply stated, there is no evidence that mafic magma has progressively crystallized or evolved by any monotonic process toward compositions richer in silica, volatiles, or radiogenic Sr over the last 350 kyr (Fig. 9b).

Generation of zoned magma beneath Volcán San Pedro may have a parallel at Cerro Azul–Quizapu, located 45 km to the north of San Pedro (Fig. 1). The 1846 and 1932 eruptions of Volcán Quizapu were zoned from basalt (52 wt % SiO_2) to rhyodacite (70 wt % SiO_2); the 1846 dacitic lava contained quenched inclusions of basaltic andesite (Hildreth & Drake, 1992). The Quizapu lavas and tephras preserve coherent gradients in trace element and $^{87}Sr/^{86}Sr$ ratios similar to the zoned Younger Holocene San Pedro lavas and inclusions, i.e. the most silicic magma was less radiogenic ($^{87}Sr/^{86}Sr = 0{\cdot}70389$) than the basaltic end-member (0·70404; Hildreth & Drake, 1992). Further work will be needed to establish whether our interpretation of partial melting of young, unradiogenic hornblende–phlogopite gabbro in response to influx of relatively radiogenic basalt may apply to Quizapu and possibly other Holocene to Recent eruptions throughout the Andean SVZ.

SUMMARY AND CONCLUSIONS

From field, petrographic, geochemical, and isotopic observations we propose the following model for the Younger Holocene San Pedro magmas (Fig. 11):

(1) dacite was generated by dehydration partial melting of relatively young gabbroic rocks with unradiogenic Sr similar to the hornblende–phlogopite gabbroic xenoliths found in the dacite.

(2) Forceful injection of basaltic magma dispersed blobs of quenched basaltic magma into the lower portion of the dacitic magma. Mingling and disaggregation of some blobs scattered olivine and plagioclase xenocrysts from the basaltic magma throughout the dacite.

(3) Olivine (Fo_{82}) and plagioclase (sieve-cored An_{84}) phyric basaltic magma ponded as its uppermost surface solidified beneath a layer of dacitic magma containing quenched blobs of basalt. The dacite was heated strongly by the cooling basalt and began to convect. Thermal changes associated with convective cycling caused repetitive cycles of An_{40} plagioclase dissolution and An_{60} growth, forming oscillatory zoned crystals with high anorthite peaks corresponding to high Mg, Fe, and Sr concentrations (Singer *et al.*, 1995). Hornblende and biotite in the lower, hotter portion of the dacitic magma became thermally unstable and dissolved or reacted with the melt.

(4) Cooling of the basalt promoted crystallization–differentiation to a basaltic andesitic composition with a temperature close enough to that of the overlying dacitic magma to permit mixing. Biotite completely dissolved and only rare hornblende relicts survived heating in the lower portion of the dacite. The upper portion of the magma body stayed sufficiently cool that these minerals remained in equilibrium. Mingling at the interface between the hybrid andesitic magma and the underlying basaltic andesitic magma produced small inclusions of quenched, differentiated basaltic andesite within the andesite.

(5) Collapse of ancestral Volcán San Pedro triggered eruption of the zoned magma body from its top down. The modern volcano is built from basaltic andesitic magma that resided beneath the zoned chamber and evolved independently from it.

Magmatism beneath Volcán San Pedro during the Holocene, and over the past 350 kyr, involved several intrusions of basalt that on occasion induced partial melting, mixing, or assimilation in the upper crust. The compositional zoning of Holocene magma at Volcán San Pedro was remarkably similar to that of historic lavas and tephras at neighboring Volcán Quizapu. The upper-crustal contributions to these magmas were not necessarily derived from SiO_2-rich granitoids. On the contrary, the importance of relatively young, hydrous gabbro in the formation of dacite and contamination of basaltic

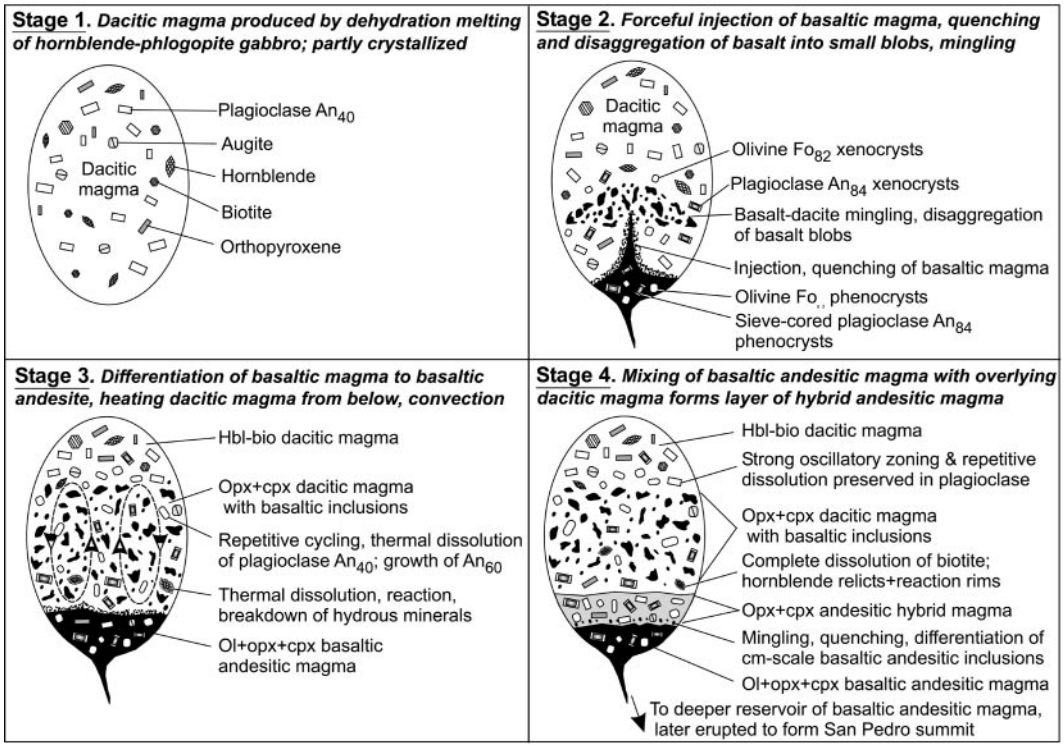


Fig. 11. Four-stage model for evolution of the zoned magma body that erupted to form the Younger Holocene composite San Pedro lava flow.

magma ascending from lower-crustal MASH zones beneath the Andean Southern Volcanic Zone may be widespread.

ACKNOWLEDGEMENTS

We extend our thanks and appreciation to Andrew Wulff, Mike Rhodes, and Fred Frey for providing the major and trace element data, and to Jon Davidson and Frank Ramos for determining Sr isotope ratios. Dwight Duering assisted with the electron microprobe analyses. We also benefited from discussion and fieldwork with Laurie Brown, Wes Hildreth, Bob Drake, Jon Davidson, Steve Nelson, Jim Pickens, and Lyn Gualtieri during the course of this project, which was initiated by Michael Dungan. We are grateful for constructive comments by Alberto Saal, an anonymous reviewer, and Associate Editor Dennis Geist, which helped us to clarify the discussion in several ways. This study was supported by the National Science Foundations of the USA and Switzerland, and a Marie Curie Fellowship from the European Community Program: Improving Human Research Potential and the Socio-Economic Knowledge Base, awarded to F.C.

REFERENCES

Bacon, C. R. (1986). Magmatic inclusions in silicic and intermediate volcanic rocks. *Journal of Geophysical Research* **91**, 6091–6112.

Bacon, C. R. & Druitt, T. H. (1988). Compositional evolution of the zoned calcalkaline magma chamber of Mt. Mazama, Crater Lake, Oregon. *Contributions to Mineralogy and Petrology* **98**, 224–256.

Bacon, C. R. & Hirschmann, M. M. (1988). Mg/Mn partitioning as a test for equilibrium between coexisting Fe–Ti oxides. *American Mineralogist* **73**, 57–61.

Bacon, C. R. & Metz, J. (1984). Magmatic inclusions in rhyolites, contaminated basalts, and compositional zonation beneath Coso volcanic field, California. *Contributions to Mineralogy and Petrology* **85**, 346–365.

Baker, M. B., Grove, T. L., Kinzler, R. J., Donnely-Nolan, J. M. & Wandless, G. A. (1991). Origin of compositional zonation (high-aluminum basalt to basaltic andesite) in the Giant Crater lava field, Medicine Lake Volcano, Northern California. *Journal of Geophysical Research* **96**, 21819–21842.

Beard, J. S. & Lofgren, G. F. (1991). Dehydration melting and water-saturated melting of basaltic and andesitic greenstones and amphibolites at 1, 3, and 6·9 kb. *Journal of Petrology* **32**, 365–401.

Bindeman, Y. N., Davis, A. M. & Drake, M. J. (1998). Ion microprobe study of plagioclase–basalt partition experiments at natural concentration levels of trace elements. *Geochimica et Cosmochimica Acta* **62**, 1175–1193.

Campbell, I. H. & Turner, J. S. (1989). Fountains in magma chambers. *Journal of Petrology* **30**, 885–923.

Costa, F. (2000). The petrology and geochemistry of diverse crustal xenoliths, Tatara–San Pedro Volcanic Complex, Chilean Andes. *Terre et Environnement* **19**, 120 pp. (Ph.D. Thesis, University of Geneva).

Costa, F., Dungan, M. A. & Singer, B. S. (2002). Hornblende- and phlogopite-bearing gabbroic xenoliths from Volcán San Pedro (36°S), Chilean Andes: evidence for melt and fluid migration and reactions in subduction-related plutons. *Journal of Petrology* **43**, 219–241.

Davidson, J. P., Dungan, M. A., Ferguson, K. M. & Colucci, M. T. (1987). Crust–magma interaction and the evolution of arc magmas: the San Pedro–Pellado volcanic complex, southern Chilean Andes. *Geology* **15**, 443–446.

Davidson, J. P., Ferguson, K. M., Colucci, M. T. & Dungan, M. A. (1988). The origin and evolution of magmas from the San Pedro–Pellado volcanic complex, S. Chile: multiple sources and open system evolution. *Contributions to Mineralogy and Petrology* **100**, 429–445.

de Silva, S. (2001). Comment on: Magmas in collision: rethinking chemical zonation in silicic magmas, by Eichelberger *et al*. *Geology* **29**, 1063.

Druitt, T. H. & Bacon, C. R. (1989). Petrology of the zoned calcalkaline magma chamber of Mt. Mazama, Crater Lake, Oregon. *Contributions to Mineralogy and Petrology* **101**, 245–259.

Dungan, M. A., Wulff, A. & Thompson, R. (2001). Eruptive stratigraphy of the Tatara–San Pedro Complex, 36°S, Southern Volcanic Zone, Chilean Andes: reconstruction method and implications for magma evolution at long-lived arc volcanic centers. *Journal of Petrology* **42**, 555–626.

Dunn, T. & Sen, C. (1994). Mineral/matrix partition coefficients for orthopyroxene, plagioclase, and olivine in basaltic to andesitic systems: a combined analytical and experimental study. *Geochimica et Cosmochimica Acta* **58**, 717–733.

Eichelberger, J. C., Chertkoff, D. G., Dreher, S. T. & Nye, C. J. (2000). Magmas in collision: rethinking chemical zonation in silicic magmas. *Geology* **28**, 603–606.

Eichelberger, J. C., Chertkoff, D. G., Dreher, S. T. & Nye, C. J. (2001). Reply to S. de Silva's comment on: Magmas in collision: rethinking chemical zonation in silicic magmas. *Geology* **29**, 1063–1064.

Feeley, T. C. & Davidson, J. P. (1994). Petrology of calc-alkaline lavas at Volcán Ollagüe and the origin of compositional diversity at Central Andean stratovolcanoes. *Journal of Petrology* **35**, 1295–1340.

Feeley, T. C. & Dungan, M. A. (1996). Compositional and dynamic controls on mafic–silicic magma interactions at continental arc volcanoes: evidence from Cordón El Guadal, Tatara–San Pedro Complex, Chile. *Journal of Petrology* **37**, 1547–1577.

Feeley, T. C., Dungan, M. A. & Frey, F. A. (1998). Geochemical constraints on the origin of mafic and silicic magmas at Cordon El Guadal, Tatara–San Pedro Complex, central Chile. *Contributions to Mineralogy and Petrology* **131**, 393–411.

Ferguson, K. M., Dungan, M. A., Davidson, J. P. & Colucci, M. T. (1992). The Tatara–San Pedro volcano, 36°S Chile: a chemically variable, dominantly mafic magmatic system. *Journal of Petrology* **33**, 1–43.

Frey, F. A., Wise, W. S., Garcia, M. O., West, H., Kwon, S.-T. & Kennedy, A. (1990). Evolution of Mauna Kea Volcano, Hawaii: petrologic and geochemical constraints on postshield volcanism *Journal of Geophysical Research* **95**, 1271–1300.

Ghiorso, M. & Sack, R. (1991). Fe–Ti oxide geothermometry: thermodynamic formulation and the estimation of intensive variables in silicic magmas. *Contributions to Mineralogy and Petrology* **108**, 485–510.

Grove, T. L., Donnelly-Nolan, J. M. & Housh, T. (1997). Magmatic processes that generated the rhyolite of Glass Mountain, Medicine Lake volcano, N. California. *Contributions to Mineralogy and Petrology* **127**, 205–223.

Grunder, A. L. & Mahood, G. A. (1988). Physical and chemical models of zoned silicic magmas: the Loma Seca Tuff and Calabozos caldera, Southern Andes. *Journal of Petrology* **29**, 831–867.

Hart, S. R. & Dunn, T. (1993). Experimental cpx/melt partitioning of 24 trace elements. *Contributions to Mineralogy and Petrology* **113**, 1–8.

Heubner, J. S. & Sato, M. (1970). The oxygen fugacity–temperature relationships of manganese nickel oxide buffers. *American Mineralogist* **55**, 934–956.

Hildreth, W. (1987). New perspectives on the eruption of 1912 in the Valley of Ten Thousand Smokes, Katmai National Park, Alaska. *Bulletin of Volcanology* **49**, 680–693.

Hildreth, W. & Drake, R. E. (1992). Volcán Quizapu, Chilean Andes. *Bulletin of Volcanology* **54**, 93–125.

Hildreth, W. & Moorbath, S. (1988). Crustal contributions to arc magmatism in the Andes of Central Chile. *Contributions to Mineralogy and Petrology* **98**, 455–489.

Hobden, B. J., Houghton, B. F., Davidson, J. P. & Weaver, S. D. (1999). Small and short-lived magma batches at composite volcanoes: time windows at Tongariro volcano, New Zealand. *Journal of the Geological Society, London* **156**, 865–868.

Kuritani, T. (2001). Replenishment of a mafic magma in a zoned felsic magma chamber beneath Rishiri Volcano, Japan. *Bulletin of Volcanology* **62**, 533–548.

Leake, B. E., Woolley, A. R., Arps, C. E. S., Birch, W. D., Gilbert, M. C., Grice, J. D., *et al.* (1997). Nomenclature of amphiboles: report of the Subcommittee on Amphiboles of the International Mineralogical Association, commission on new minerals and minerals names. *American Mineralogist* **82**, 1019–1037.

McBirney, A. R., Taylor, H. P. & Armstrong, R. L. (1987). Paricutin re-examined: a classic example of crustal assimilation in calc-alkaline magma. *Contributions to Mineralogy and Petrology*, **95**, 4–20.

Nelson, S. T., Davidson, J. P., Kowallis, B. J. & Heizler, M. T. (1999). The Tertiary tectonic history of the southern Andes: the basement to the Tatara–San Pedro volcanic complex, 36°S. *Geological Society of America Bulletin* **111**, 1387–1404.

Oldenburg, C. M., Spera, F. J., Yuen, D. A. & Sewell, G. (1989). Dynamic mixing in magma bodies: theory, simulations, and implications. *Journal of Geophysical Research* **94**, 9215–9236.

Rapp, R. P. & Watson, E. B. (1995). Dehydration melting of metabasalt at 8–32 kbar: implications for continental growth and crust–mantle recycling. *Journal of Petrology* **36**, 891–931.

Reagan, M. K., Gill, J. B., Malavassi, E. & Garcia, M. O. (1987). Changes in magma composition at Arenal volcano, Costa Rica, 1968–1985: real-time monitoring of open-system differentiation. *Bulletin of Volcanology* **49**, 415–434.

Rhodes, J. M. (1988). Geochemistry of the 1984 Mauna Loa eruption: implications for magma storage and supply. *Journal of Geophysical Research* **93**, 4453–4466.

Rollinson, H. R. (1993). *Using Geochemical Data: Evaluation, Presentation, Interpretation.* Harlow: Longman; New York: Wiley, 352 pp.

Rutherford, M. J. & Hill, P. M. (1993). Magma ascent rates from amphibole breakdown: an experimental study applied to the 1980–1986 Mount St. Helens eruptions. *Journal of Geophysical Research* **98**, 19667–19685.

Scaillet, B. & Evans, W. E. (1999). The 15 June 1991 eruption of Mount Pinatubo. I. Phase equilibria and pre-eruption P–T–fO_2–fH_2O conditions of the dacite magma. *Journal of Petrology* **40**, 381–411.

Sen, C. & Dunn, T. (1994). Dehydration melting of a basaltic composition amphibolite at 1·5 and 2·0 GPa: implications for the origin of adakites. *Contributions to Mineralogy and Petrology* **117**, 394–409.

Singer, B. S., Dungan, M. A. & Layne, G. D. (1995). Textures and Sr, Ba, Mg, Fe, K, and Ti compositional profiles in volcanic plagioclase: clues to the dynamics of calc-alkaline magma chambers. *American Mineralogist* **80**, 776–798.

Singer, B. S., Thompson, R. A., Dungan, M. A., Feeley, T. C., Nelson, S. T., Pickens, J. C., Brown, L. L., Wulff, A. W., Davidson, J. P. & Metzger, J. (1997). Volcanism and erosion during the past 930 k.y. at the Tatara–San Pedro complex, Chilean Andes. *Geological Society of America Bulletin* **109**, 127–142.

Singer, B., Hildreth, W. & Vincze, Y. (2000). $^{40}Ar/^{39}Ar$ evidence for early deglaciation of the central Chilean Andes. *Geophysical Research Letters* **27**, 1663–1666.

Sisson, T. W. (1994). Hornblende–melt trace-element partitioning measured by ion-microprobe. *Chemical Geology* **117**, 331–344.

Smith, D. R. & Leeman, W. P. (1987). Petrogenesis of Mount St. Helens dacitic magmas. *Journal of Geophysical Research* **92**, 10313–10334.

Snyder, D. & Tait, S. (1998). The imprint of basalt on the geochemistry of silicic magmas. *Earth and Planetary Science Letters* **160**, 433–445.

Sparks, R. S. J. & Marshall, L. A. (1986). Thermal and mechanical constraints on mixing between mafic and silicic magmas. *Journal of Volcanology and Geothermal Research* **29**, 99–124.

Tepper, J. H., Nelson, B. K., Bergantz, G. W. & Irving, A. J. (1993). Petrology of the Chilliwack Batholith, North Cascades, Washington: generation of calc-alkaline granitoids by melting of mafic lower crust with variable water fugacity. *Contributions to Mineralogy and Petrology* **113**, 333–351.

Tsuchiyama, A. (1985). Dissolution kinetics of plagioclase in the melt of the system diopside–albite–anorthite, and the origin of dusty plagioclase in andesites. *Contributions to Mineralogy and Petrology* **89**, 1–16.

Turner, J. S. & Gustafson, L. B. (1981). Fluid motions and compositional gradients produced by crystallization or melting at vertical boundaries. *Journal of Volcanology and Geothermal Research* **11**, 93–125.

Turner, S. P., George, R. M. M., Evans, P. J., Hawkesworth, C. J. & Zellmer, G. F. (2000). Time-scales of magma formation, ascent and storage beneath subduction-zone volcanoes. *Philosophical Transactions of the Royal Society of London, Series A* **358**, 1443–1464.

Wilcox, R. E. (1954). Petrology of Parícutin Volcano, Mexico. *US Geological Survey Bulletin* **965-C**, 281–353.

Wolf, M. B. & Willie, P. J. (1994). Dehydration-melting of amphibolite at 10 kbar: the effects of temperature and time. *Contributions to Mineralogy and Petrology* **115**, 369–383.

APPENDIX

Table A1: Ranges of partition coefficients used in Rayleigh crystallization and batch melting models

	olivine	clinopyroxene	orthopyroxene	hornblende	plagioclase*	magnetite	apatite
K	0·007	0·007–0·037	0·002	0·08–0·3	0·07–0·08	0·001	0·01
Rb	0·001–0·009	0·032	0·003	0·014–0·04	0·01–0·02	0·01	0·01
Ba	0·006–0·01	0·0007–0·131	0·003	0·044–0·1	0·15–0·25	0·01	0·01
La	0·0038	0·054–0·3	0·002–0·08	0·26–0·5	0·14–0·16	0·15–0·22	14·5
Sr	0·014–0·18	0·13–0·516	0·005–0·009	0·3–0·49	2–2·8	0·01	0·01
Zr	0·001–0·012	0·12–0·6	0·2	0·31–0·34	0·01	0·01–0·2	0·01
Y	0·01–0·033	0·47–1·9	0·36–0·45	2·5–6	0·03–0·04	0·05–0·5	35
Yb	0·001–0·014	0·43–1·58	0·65–0·86	1·3–4·9	0·05	0·11–0·25	15·4

*$An_{50–60}$.

Data sources: mostly from the compilation of Rollinson (1993). Other sources: Hart & Dunn (1993), Dunn & Sen (1994), Sisson (1994), and Bindeman *et al.* (1998).